THE ASTROPHYSICAL JOURNAL, 385:173–187, 1992 January 20

ORIGIN OF THE STRUCTURES AND POLARIZATION IN THE CLASSICAL DOUBLE 3C 219

DAVID A. CLARKE[1]
Institute for Astrophysics, University of New Mexico; and National Center for Supercomputing Applications, The Beckman Institute, Drawer 25, University of Illinois at Urbana-Champaign, Urbana, IL 61801

ALAN H. BRIDLE
National Radio Astronomy Observatory, Edgemont Road, Charlottesville, VA 22903-2475

JACK O. BURNS[1]
Department of Astronomy, New Mexico State University, Box 30001, Department 4500, Las Cruces, NM 88003

RICHARD A. PERLEY
National Radio Astronomy Observatory, P.O. Box 0, Socorro, NM 87801

AND

MICHAEL L. NORMAN
National Center for Supercomputing Applications, The Beckman Institute, Drawer 25, University of Illinois at Urbana-Champaign, Urbana, IL 61801
Received 1991 March 22; accepted 1991 August 2

ABSTRACT

Scaled-array VLA observations of the "classical double" radio galaxy 3C 219 at 1.4, 1.5, 1.7, and 4.9 GHz with 1".4 resolution have been used to derive the spectral and polarimetric properties of the source. The extended emission of the lobes is filamentary, as in other well-resolved radio galaxies. A second type of filamentation, spatially independent of the total intensity filaments, is found in the depolarization distribution of the source. The depolarization filaments are associated with strong local gradients in the rotation measure and may indicate that a clumpy magnetoionic medium surrounds the radio galaxy.

3C 219 is one of the few Fanaroff-Riley Class II radio sources known in which there is direct evidence for a counterjet. Both the counterjet and main jet are "partial jets," i.e., they seem to disappear long before reaching the hot spot in their associated lobes. The disappearance of the main jet is accompanied by a transition from an axial to a transverse magnetic field along the jet axis. Two interpretations for the abbreviated nature of the jets are considered. The "born-again, relativistic jet" model assumes an episodic behavior in the relativistic outflow from the radio core. The "passive magnetic field" model relates the observed asymmetries between the two jets to different orientations of the passive magnetic field that they transport. The strengths and weaknesses of each model as applied to 3C 219 are discussed.

Finally, the observations are compared with numerical simulations of propagating jets with both active (dynamically important) and passive (dynamically negligible) magnetic fields.

Subject headings: galaxies: individual (3C 219) — galaxies: jets — polarization — radio continuum: galaxies

1. INTRODUCTION

The classical double radio galaxy 3C 219 (R.A.[1950] = $9^h17^m50^s.6$, decl.[1950] = 45°51′44″, $P_{1400\,\mathrm{MHz}} \sim 3 \times 10^{26}$ W Hz^{-1}) is optically identified with a 17.5 mag cD galaxy (Matthews, Morgan, & Schmidt 1964) with a redshift of 0.1745 (Schmidt 1965), corresponding to a distance of $410h_{100}^{-1}$ Mpc (where $h_{100} \equiv H_0/100$ [km s^{-1} Mpc^{-1}], and $q_0 = 0$). It is the brightest member of a compact Zwicky cluster in the southeast corner of Ursa Major (Macdonald, Kenderdine, & Neville 1968).

Previous VLA observations by Perley et al. (1980, hereafter PBWF) and Bridle, Perley, & Henriksen (1986, hereafter BPH) revealed 3C 219 as one of the few classical doubles known to possess a jet that disappears along the path between the radio core and the terminal hot spot in its associated lobe. The images of BPH also revealed for the first time a single elongated knot on the path where a counterjet may be expected. This counterjet knot is resolved and is brightest on its lobeward edge. If reflected through the core, it would lie in the apparent "gap" in the radio emission at the base of the main jet. BPH considered both the "flip-flop" model and "born-again relativistic jet" model to explain the apparent failure of both jets to reach their respective terminal hot spots. These models may both be considered members of a class of "restarting jet" models which are examined in detail in § 5.

BPH showed that the brightest parts of the main jet are "overpressured" relative to the plausible model-dependent pressures of the ambient cluster medium and offered two interpretations of this result. In the first interpretation, the brightest jet knots are overpressured by shocks driven into the flow as it is recollimated by the atmosphere of the cluster containing 3C 219. In the second interpretation, the jet is partially collimated by the $J \times B$ forces arising from the interaction of an active (dynamically important) toroidal magnetic field and an axial current density transported by the jet. BPH noted two ways in which such magnetically assisted collimation could be consistent with the nearly axial configuration of the apparent magnetic field $\boldsymbol{B}_a$ which they deduced from their polarimetry of the jet. First, the jet might be too poorly resolved to observe the pattern of fractional polarization and apparent field orien-

[1] Guest Observer of the National Radio Astronomy Observatory, which is operated by Associated Universities Inc., under cooperative agreement with the National Science Foundation.

tation expected of a helical magnetic field. Second, the confining magnetic field might lie in the cocoon surrounding the bright jet as suggested by Begelman, Blandford, & Rees (1984). BPH proposed that the second alternative could be investigated by sensitive polarimetry of the cocoon in 3C 219 at frequencies for which the medium surrounding the jet has enough Faraday depth to produce observable rotation measure gradients.

This paper reports the results of such a study using the VLA to obtain 1".4 resolution at 1.4, 1.5, 1.7, and 4.9 GHz. The results are compared with total and polarized synchrotron emission images computed from numerical simulations of propagating jets with passive (dynamically negligible) magnetic fields (Clarke, Norman, & Burns 1989, hereafter CNB) and of jets with active magnetic fields (Norman, Clarke, & Burns 1987; Clarke 1988).

The outline of this paper is as follows, Section 2 discusses the new VLA observations and their reduction, while § 3 presents the data. Section 4 examines "restarting jet" models in which the disappearance of the jet is linked to temporal changes in the energy flow from the central engine. Section 5 examines the hydrodynamical, passive magnetic field model of CNB, which suggests an alternate interpretation of the disappearance of the jet in 3C 219. Finally, § 6 summarizes the major results.

2. THE DATA REDUCTION

Previous VLA observations (from PBWF and BPH) include 6 cm data in the A, B/C hybrid, and C configurations, and 20 cm data in the A, B, and C configurations. Only in the A configuration was the source observed continuously for a substantial time. The B and C configuration data consist of "snapshots" obtained during other observing programs, so the u-v coverage is sparse at the shorter baselines and some extended structure is poorly sampled or missing. All of these observations were made with a 50 MHz bandwidth, introducing some severe bandwidth smearing (chromatic aberration) for fine detail in the outer parts of the source at 20 cm.

These earlier VLA data were supplemented with new 6 cm data in the B configuration of the VLA and 18 and 22 cm data in the A and B configurations. Two calibrators were used for all the observations. To put the observations on the scale of Baars et al. (1977), 3C 286 was used as the absolute flux density and polarization calibrator. The local calibrator 0917+449 was observed every 30 minutes to monitor instrumental and atmospheric fluctuations. To reduce the effects of bandwidth smearing, a 25 MHz bandwidth was used for the new observations. At 70" from the phase center (approximately the distance from the core to either of the hot spots in the lobes), this bandwidth produces a 3% and 14% peak intensity attenuation and associated radial beam smearing, for 6 cm and 22 cm, respectively (e.g., Thompson & D'Addario 1982). Table 1 summarizes the new observations and those of PBWF and BPH.

The data were first calibrated with the local calibrator. Each data base was then self-calibrated (Schwab 1980), imaged (Fourier transformed), and CLEANed (Clark 1980) using the Astronomical Image Processing System (AIPS) maintained by the NRAO. The A and B configuration data at 22 cm were then combined, self-calibrated further, imaged, and CLEANed. The 18 cm data bases were reduced similarly. The A and B configuration data of PBWF and BPH were combined to produce a third image, at 20 cm. Finally, the new 6 cm B configuration data were combined with the B/C and C configuration data of PBWF and BPH. To compensate partially for the lack of shorter spacings in the 6 cm data (Table 1), a zero-spacing flux density of 2.2 Jy (estimated by extrapolating the plot of flux density vs. baseline to zero baseline) was added to the 6 cm data during the data processing.

Before one can meaningfully interpret multifrequency images such as the spectral index (α, defined here by $I_\nu \propto \nu^{-\alpha}$), one must first investigate the effects of differences among the u-v coverages at the frequencies involved. For these observations, the differences in the u-v coverages at 6 and 22 cm arise because the short spacings in the 6 cm data of BPH are from several snapshots while those in the new data at 18 and 22 cm are from a full synthesis.

To test the credibility of the spectral index between 6 and 22 cm, a "false" 3C 219 was created. Using standard software available in AIPS, 2.5 Jy of flux density (comparable to the known total flux density of the source at 6 cm) were distributed among a single point source and four Gaussian components with elliptical cross sections. These components were positioned at the centroids of the major features in 3C 219 and, together, crudely reproduce the gross structures of the source. The "false" 3C 219 was overwritten onto the visibilities of both the 22 cm A+B configuration data and the 6 cm B+B/C+C configuration data to determine how the u-v coverage samples the known intensity distribution. Each

TABLE 1

SUMMARY OF OBSERVATIONS FOR 3C 219

Date	ν (MHz)	λ (cm)	VLA Array	Projected Baseline Range (kλ)	3C 286 (Jy)	0917+449 (Jy)	Hour Angle Range	Observation Time (hr)
1978 Sep 29[a]	4885	6	B/C[b]	2.1–179	7.41	0.80	..., ...	6.0
1978 Sep 30[a]	1480	20	B/C[b]	0.5–52	14.43	0.66	..., ...	5.0
1982 Aug 29[c]	1465	20	A	1.6–168	14.50	...	..., ...	2.0
1983 Feb 10[c]	4885	6	C	1.2–55	7.41	...	..., ...	1.0
1986 May 18	1385	22	A	3.3–169	14.91	0.817	$+4^h.2$, $-4^h.6$	6.0
	1665	18	A	4.0–203	13.61	0.874	+4.2, −4.6	6.0
1986 Sep 6	1385	22	B	0.31–52	14.91	0.806	+6.2, −7.6	6.5
	1665	18	B	0.37–62	13.61	0.886	+6.2, −7.6	6.5
	4873	6	B	2.1–179	7.42	1.089	+7.2, −6.5	5.0
	4823	6	B	1.8–172	7.47	1.087	+7.2, −6.5	5.0

[a] Data courtesy of PBWF.
[b] Only 12 antennas were available in the partially completed array.
[c] Data courtesy of BPH.

"false" data base was imaged with a zero spacing flux density of 2.5 Jy and deconvolved with 50,000 CLEAN components. Two conclusions were drawn by comparing the images from the two "false" data bases. First, the 22 cm "false" image distributes all the known flux density correctly among the components. This shows that the 22 and 18 cm u-v coverages are complete enough to represent the absolute flux densities of all parts of 3C 219 correctly to within an estimated calibration uncertainty of about 5%. Second, the apparent spectral indices between 6 and 22 cm of the most extended structures are probably too high, by as much as 0.4. The spectral indices of the compact features and of the brighter subregions of the extended structures can be trusted, however.

A different potential source of error affects the polarization data. As discussed by Dreher, Carilli, & Perley (1987), the observed fractional polarization can be attenuated by two effects, both of which are sometimes called "beam depolarization." The first effect occurs if the beam underresolves intrinsic detail in the Stokes Q and U distributions in the source, e.g., local fluctuations in the magnetic field geometry. The CLEAN beam then combines different orientations of the polarization pseudovector, giving a net polarization less than that which would be observed at higher resolution. Such *geometrical* beam depolarization is independent of the wavelength provided there is no substantial gradient in the true depolarization over the source itself. The second type of beam depolarization results from strong, unresolved gradients in the rotation measure of a Faraday screen. This can depolarize the signal even where the orientation of the intrinsic (zero-wavelength) polarization is uniform. This *Faraday* beam depolarization inherits the wavelength dependence of Faraday rotation. As discussed by Burn (1966), Milne (1980), and Laing (1985), Faraday beam depolarization can lead to depolarization whose variation with wavelength depends on the distribution of unresolved scale sizes in the Faraday screen [the observed polarized intensity $\propto \exp(-\lambda^4)$ if the unresolved fluctuations have a unique scale]. Faraday beam depolarization is therefore potentially more damaging at low frequencies. Gradients in the rotation measure must, however, be ≥ 150 rad m^{-2} across a single CLEAN beam before Faraday beam depolarization exceeds 5% at 6 cm (see Dreher et al. 1987). The RM data suggest that Faraday beam depolarization is small at all but a few locations in 3C 219 (§ 3.2).

To test whether the polarization data might suffer from geometrical beam depolarization, the 22 cm data were tapered with a Gaussian function falling to 30% at 50 kλ, and Stokes I, Q, and U images were created with a CLEAN beam of FWHM 2".7 (roughly twice the CLEAN beam FWHM of the untapered images). The corresponding lower resolution fractional polarization image was then divided by the full resolution fractional polarization image to create an image that estimates the geometrical depolarization at 2".7 resolution. If the polarization structure of the more extended regions of 3C 219 is *amply* resolved at 1".4 FWHM, the geometrical depolarization values on the test image should be near unity everywhere. Over modest regions (20"–40" on a side), they are between 0.8 and 0.9, however, and in the southern portion of the northern lobe, they are as low as 0.55. It is therefore possible that geometrical beam depolarization depresses the observed fractional polarization over some of 3C 219, even at 1".4 resolution. This possibility can be tested only by aberration-free high-resolution data on the lobes, which are not currently available.

Table 2 lists some parameters of the four multiconfiguration images. Because of the slightly differing CLEAN beam sizes, the 6, 18, and 22 cm Stokes I, Q, and U images were each convolved with a 1".4 circular beam before making the comparison images such as spectral index, depolarization, and RM. The larger CLEAN beam of the 20 cm data was not artificially reduced to 1".4 since these data were used for the rotation measure experiment only.

3. THE DATA

Figures 1 and 2 (Plates 5 and 6) are gray-scale total intensity images at 6 and 22 cm, respectively. The resolution (FWHM) of these and, unless otherwise stated, all other images in this paper is 1".4, corresponding to a linear scale of $2.8h_{100}^{-1}$ kpc. The features labeled in Figure 1 include an elliptical hot spot in the northern lobe (N2), the single knot just northeast of the core which BPH identify as the brightest part of a counterjet (N1), the radio core (C), the knots in the main jet (features S1–S8), and an elongated, L-shaped hot spot in the southern lobe (S9). Figure 3 (Plate 7) shows new gray-scale renditions of these features created from the high-resolution (0".4, $800h_{100}^{-1}$ pc FWHM) 6 cm data of BPH. In addition, a small classical double (dubbed "Baby 219" because of its very similar appearance and orientation to 3C 219 itself) is visible on Figure 1. The

TABLE 2

THE MULTICONFIGURATION IMAGES OF 3C 219

VLA Arrays	λ (cm)	Beam FWHM[a]	CLEANed Flux Density (Jy)	I_{max}[b]	RMS$_I$[c]	P_{max}[d]	RMS$_P$[e]
B+B/C+C	6	1".2 × 1".0 PA = −82°.6	1.91	49.9	32	5.3	30
A+B	18	1".1 × 0".98 PA = −7°.7	5.96	41.1	44	10.3	33
A+B	20	1".6 × 1".5 PA = −58°.1	7.48	71.4	77	12.2	71
A+B	22	1".3 × 1".2 PA = −10°.1	7.15	58.6	46	13.8	36

[a] Full width at half-maximum of CLEAN beam (resolution); PA = position angle of major axis of CLEAN beam counterclockwise from north.
[b] Peak total brightness on image (mJy per CLEAN beam).
[c] RMS noise on total intensity image (μJy per CLEAN beam).
[d] Peak polarised brightness on image (mJy per CLEAN beam).
[e] RMS noise on polarized intensity image, with Riccian correction (μJy per CLEAN beam).

1992ApJ...385..173C

TABLE 3

3C 219 RADIO PARAMETERS

Feature	I_{22}[a] (mJy)	I_{18}[b] (mJy)	I_6[c] (mJy)	α_{18}^{22}[d]	α_6^{18}[e]	RM[f] (rad m^{-2})	f_{22}[g]	f_{18}[h]	f_6[i]	d_{18}^{22}[j]	d_6^{18}[k]
N2[l]	326.8 ± 0.7	287.8 ± 0.6	120.8 ± 0.5	0.69 ± 0.02	0.811 ± 0.005	−1. ± 12.0	0.196 ± 0.002	0.197 ± 0.002	0.209 ± 0.004	1.00 ± 0.01	0.94 ± 0.02
N1	5.36 ± 0.07	4.78 ± 0.06	1.96 ± 0.05	0.62 ± 0.10	0.83 ± 0.03	...	0.057 ± 0.010	0.059 ± 0.010	0.060 ± 0.021	0.97 ± 0.23	0.99 ± 0.39
C	37.32	37.00	50.55	0.05 ± 0.02	−0.292 ± 0.002	...	0.003 ± 0.001	0.003 ± 0.001	0.0041 ± 0.0008	1.0 ± 0.7	0.65 ± 0.34
S1	13.02	11.48	5.62	0.68 ± 0.04	0.67 ± 0.01	+0.4 ± 0.3	0.156 ± 0.004	0.170 ± 0.004	0.228 ± 0.008	0.92 ± 0.03	0.75 ± 0.03
S3	14.86	12.53	5.49	0.93 ± 0.04	0.77 ± 0.01	−6.2 ± 0.2	0.280 ± 0.004	0.284 ± 0.004	0.368 ± 0.008	0.98 ± 0.02	0.78 ± 0.02
S8	26.93	23.40	10.97	0.76 ± 0.02	0.708 ± 0.005	−6.8 ± 0.2	0.192 ± 0.002	0.190 ± 0.002	0.203 ± 0.004	1.01 ± 0.02	0.93 ± 0.02
S9[l]	359.1 ± 0.6	308.1 ± 0.5	139.5 ± 0.4	0.83 ± 0.02	0.740 ± 0.004	−14. ± 2.0	0.102 ± 0.002	0.096 ± 0.002	0.105 ± 0.003	1.06 ± 0.02	0.91 ± 0.03
BC	0.41 ± 0.07	0.30 ± 0.06	0.34 ± 0.05	1.7 ± 1.5	−0.13 ± 0.23	...	...	...	...	...	...

[a] Flux density at 22 cm.
[b] Flux density at 18 cm.
[c] Flux density at 6 cm.
[d] Spectral index between 18 and 22 cm. Add 0.08 to each uncertainty to account for the calibration error.
[e] Spectral index between 6 and 18 cm. Add 0.07 to each uncertainty to account for the calibration error.
[f] Rotation measure.
[g] Fractional polarization at 22 cm.
[h] Fractional polarization at 18 cm.
[i] Fractional polarization at 6 cm.
[j] Depolarization (f_{22}/f_{18}).
[k] Depolarization (f_{18}/f_6).
[l] Resolved feature.

northern lobe, core, and southern lobe of Baby 219 are labeled BN, BC, and BS respectively.

Table 3 contains radio data for some features in 3C 219. Because much of the emission from Baby 219 is badly confused with 3C 219 (especially at 18 and 22 cm), estimates of flux densities, spectral indices, etc. for this source are unreliable, except for the core. Estimated contributions from the background have been removed from all flux densities. In principle, the uncertainty in the flux densities consists of the rms noise levels in the images, an uncertainty associated with the subtraction of the background (the rms noise is a lower limit), and a calibration error, estimated to be 5% for these databases. Since the calibration error is systematic and not random like the rms noise, it should not be used in determining the uncertainties for derived quantities such as the spectral index gradient, fractional polarization, etc. Thus, the uncertainties in Table 3 are derived from $\sqrt{2}$ times the total intensity rms noise levels given in Table 2. Note that this underestimates the uncertainties in the *absolute* spectral indices since the calibration errors are relevant in this case.

For resolved features, the flux densities reported in Table 3 are integrated over the feature and these are used to determine the quoted values of the spectral index, fractional polarization, and depolarization. The uncertainties quoted with these quantities are determined by formally propagating the integrated flux density uncertainties. Conversely, the rotation measure and its uncertainty are respectively determined from the arithmetic mean and the standard deviation of the RM over the feature. For unresolved features, the reported flux density is integrated over a single CLEAN beam and the quoted uncertainties in all derived quantities are determined by formally propagating the relevant uncertainties.

3.1. *Total Intensity and Spectral Index*

The integrated flux density of the southern lobe ($F_{22} = 3.97$ Jy, $F_{18} = 3.56$ Jy, and $F_6 \gtrsim 1.0$ Jy) is slightly greater than that of the northern lobe ($F_{22} = 3.75$ Jy, $F_{18} = 3.29$ Jy, and $F_6 \gtrsim 0.9$ Jy) at all wavelengths. Together, the lobes of 3C 219 span about $370h_{100}^{-1}$ kpc in the plane of the sky. In Figure 2, the lobes are seen to be filamentary, as in other well-resolved radio galaxies such as Hercules A (Dreher & Feigelson 1984), Cygnus A (Perley, Dreher, & Cowan 1984), Centaurus A (Clarke 1988), and M87 (Hines, Owen, & Eilek 1989). These filaments are equally prominent on images of 3C 219 deconvolved using maximum entropy methods (MEM, e.g., Cornwell & Evans 1985). It is therefore unlikely that the filaments are artifacts of CLEAN instabilities (Cornwell 1983) or other defects of the deconvolution.

In contrast to those in M87, the total intensity filaments in 3C 219 are not overpressured relative to the thermal pressure in a plausible intracluster medium (BPH). The brightness at 22 cm of the brightest filaments in 3C 219 is 20%–25% (about 1 mJy per CLEAN beam) above the brightness in the interfilament region. The spectral index between 6 and 18 cm in the filaments ranges from 0.6 to 1.0, and the deconvolved width of the filaments ranges from 1″ to 3″. If the observed widths of the filaments are similar to their dimensions along the line of sight, then these observations correspond to a minimum pressure of about 2.0×10^{-13} N m^{-2}. This is an order of magnitude *less* than the minimum pressure found anywhere along the jet (Table 4) and about two orders of magnitude less than the minimum pressure in the brightest parts of the jet as determined by the high-resolution data of BPH. Thus, an intracluster medium that can confine the jet would also confine the total

TABLE 4

3C 219 EQUIPARTITION CALCULATIONS

Feature	σ[a]	B_{mp}[b] (T)	e_{mp}[c] (J m^{-3})	p_{mp}[d] (N m^{-2})	τ_{syn}[e] (yr)
18 and 22 Centimeters					
N2[f]	12″	9.7×10^{-10}	5.0×10^{-13}	1.7×10^{-13}	3.7×10^{7}
N1	1.4	1.8×10^{-9}	1.7×10^{-12}	5.8×10^{-13}	1.4×10^{7}
S1	1.4	2.4×10^{-9}	3.1×10^{-12}	1.0×10^{-12}	9.3×10^{6}
S3	1.4	3.0×10^{-9}	4.8×10^{-12}	1.6×10^{-12}	6.7×10^{6}
S8	1.4	3.1×10^{-9}	5.2×10^{-12}	1.7×10^{-12}	6.3×10^{6}
S9[f]	5	2.3×10^{-9}	2.8×10^{-12}	9.5×10^{-13}	9.9×10^{6}
Filament	...	1.1×10^{-9}	6.0×10^{-13}	2.0×10^{-13}	3.2×10^{7}
Lobe	...	8.9×10^{-10}	4.2×10^{-13}	1.4×10^{-13}	4.2×10^{7}
6 and 18 Centimeters					
N2[f]	12″	1.1×10^{-9}	6.4×10^{-13}	2.1×10^{-13}	2.8×10^{7}
N1	1.4	2.1×10^{-9}	2.3×10^{-12}	7.8×10^{-13}	1.0×10^{7}
S1	1.4	2.4×10^{-9}	3.1×10^{-12}	1.0×10^{-12}	8.6×10^{6}
S3	1.4	2.6×10^{-9}	3.7×10^{-12}	1.2×10^{-12}	7.4×10^{6}
S8	1.4	3.0×10^{-9}	4.8×10^{-12}	1.6×10^{-12}	6.1×10^{6}
S9[f]	5	2.2×10^{-9}	2.5×10^{-12}	8.3×10^{-13}	1.0×10^{7}
Filament	...	1.0×10^{-9}	5.7×10^{-13}	1.9×10^{-13}	3.0×10^{7}
Lobe	...	8.9×10^{-10}	4.2×10^{-13}	1.4×10^{-13}	4.0×10^{7}

[a] Angular diameter of feature.
[b] Equipartition magnetic field.
[c] Equipartition internal energy density.
[d] Equipartition minimum pressure.
[e] Synchrotron lifetime of the electrons.
[f] Resolved feature.

intensity filaments in the lobes. These data, therefore, do not necessarily imply that the filaments in the lobes of 3C 219 are shocks. In addition, if the observed widths of the lobes (40″) are similar to their dimensions along the line of sight, these data imply that the emissivity of the filaments are 3–8 times greater than the interfilament emissivity, and that the filling factors of the filaments are between 0.03 and 0.08. Thus, these data are consistent with the model proposed by Norman et al. (1987) in which large-scale transonic turbulence in the lobe entrains "dark" ambient material (i.e., material with little or no synchrotron emissivity) producing filaments as the two media mix.

Figure 4 (Plate 8) is an inverse gray-scale image of the spectral index between 6 and 18 cm (bright regions correspond to low spectral indices). Data are shown only where the brightness in both images exceeds 3 times the estimated rms noise (Table 2). As discussed in the previous section, the spectral index between 6 and 18 cm is probably realistic in the brighter regions of the lobes and in the small-scale features, but it is almost certainly too high in the extended diffuse regions, particularly in the cocoon surrounding the jet and the radio core. A spectral index image between 18 and 22 cm (not shown) was also created, yielding useful low-frequency spectral data in the regions of bright emission (see Table 3). The high-frequency spectral index (α_6^{18}) of the extended emission steepens dramatically (from ~ 0.8 to > 1.6; Fig. 4) from the hot spots toward the core. This is consistent with an electron population that ages in the absence of strong reacceleration processes, as proposed by Dreher et al. (1987) for Cygnus A. Some of the apparent steepening in the spectral index in this region of 3C 219 can also be attributed to the incomplete *u-v* coverage at 6 cm, however. The spectral index data for 3C 219 also contain a qualitatively new feature—"fans" of relatively lower spectral index emanating from each hot spot toward the edges of their respective lobes (see Fig. 4). In these features, α_6^{18} is typically less than but close to unity with an uncertainty of several percent. These fanlike regions cannot be an artifact of incomplete *u-v* coverage. Furthermore, because they are well resolved, they cannot be an artifact of chromatic aberration. They may therefore trace the outflow of the thermalized, transonic jet material after being shocked by the terminal Mach disk (hot spot). Having been recently energized by the shock, the relativistic particles in the fans would emit radiation with a lower spectral index than older particles in regions further downstream from the hot spots.

In the northern lobe, the low-frequency spectral indices of the compact features (N1 and N2) are significantly less than the high-frequency spectral indices (see Table 3), as might be expected from the standard synchrotron model. However, in the southern lobe, the situation is reversed. The low-frequency spectral indices of all the compact features (with the possible exception of S1) are *greater* than the high-frequency spectral indices. The different spectral behavior of the compact features in the two lobes is evident even without the background subtraction. The spectral data at the two cores (C and BC) are consistent with a flat low-frequency spectrum and an inverted high-frequency spectrum.

The northern hot spot (N2) is, on average, 12″ ($24 h_{100}^{-1}$ kpc) in diameter. The high resolution total intensity image of the feature (Fig. 3 [*top right*]) reveals considerable internal structure, including an edge-brightened rim and a bright central peak. The surface brightness around the rim is not uniform—the north and east sides are much brighter than the south and west. The bright portion of the rim is almost circular, but the dim western perimeter traces an elliptical shape. Little of this internal structure is evident in the spectral index image in Figure 4, and the data are consistent with a uniform spectral index across the hot spot.

As reported by BPH, the main jet is straight and exhibits a wealth of internal structure (Fig. 3*b*; 3 [*left*]; see also Fig. 9*b* in which all of the major features are labeled). There is a 7° bend in the vicinity of S4 and a pronounced wiggle at the end of the jet where knot S8 resembles a "hook." The "gap" between the core and S1 is not truly empty of radio emission. A faint V-shaped emission feature joins the core to the main jet (Fig. 2). This feature is unresolved—its V-shape is an artifact of the systematic increase in intensity between the core and S1 (Fig. 14*a*) rather than of a systematic lateral expansion. While this feature may represent the rapidly spreading portion of the jet hypothesized by BPH, there is no direct evidence of lateral expansion from these data to confirm this.

The width of the jet varies considerably along its length. Figure 5*a* shows the FWHM of the jet as a function of distance from the core, with the locations of the knots indicated. These

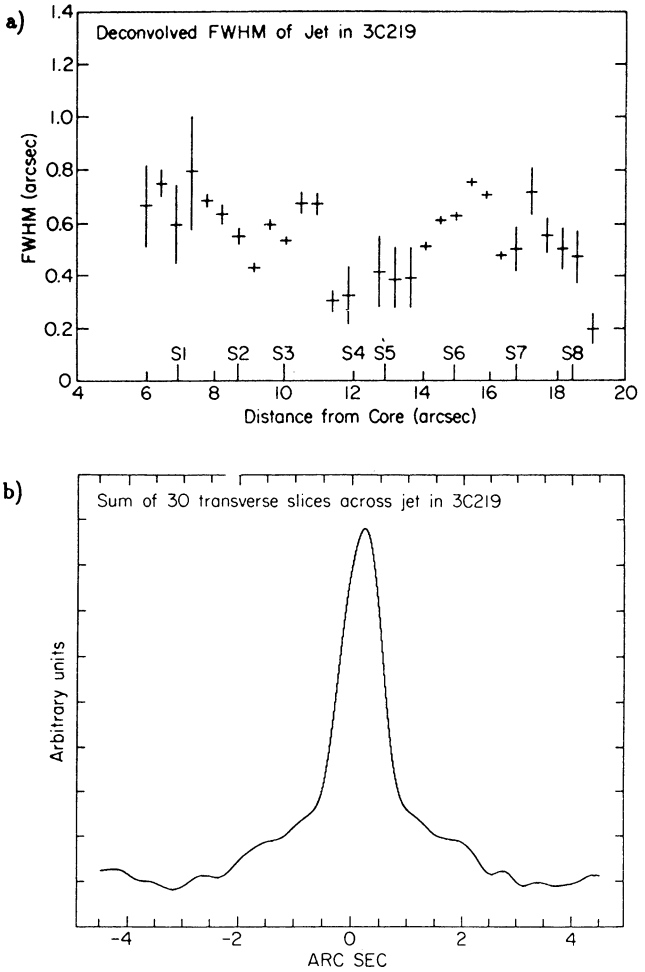

FIG. 5.—(*a*) The full width half-maximum of Gaussian functions fitted to transverse profiles across the jet as a function of distance from the radio core using the high-resolution (6 cm, 0.″35) data of BPH. (*b*) The aggregate of all the profiles used to produce (*a*). At least two components of the emission can be identified—the jet (FWHM 0.″9, broadened in this summation by the nonlinearity of the jet path) and the cocoon (FWHM 3″).

FWHM values were determined by fitting Gaussian functions and curvilinear "baselines" to transverse profiles across the jet using the high-resolution (0".4) 6 cm data of BPH. If the jet outflow is traced by the synchrotron emission, then the jet undergoes at least four periods of expansion and contraction before it disappears. The strong contraction between knots S7 and S8 is particularly notable. Figure 5*b* shows the sum of all the transverse profiles used to produce Figure 5*a*. This represents an "average" transverse profile along the length of the jet and suggests that the jet consists of at least two components. The narrow feature with a FWHM of 0".9 is the bright jet (broadened slightly here by the nonlinearity of the jet path). The feature with a FWHM of about 3" is a broad, faint "inner cocoon" in which the jet is embedded. There is no evidence for a systematic lateral expansion of this "inner cocoon" component.

The abruptness with which the jet emission stops after knot S8 is striking. The transition between the jet and the background emission is still unresolved in the 0".4 resolution image (Fig. 3*b*). To examine this region in more detail, a MEM deconvolution of the BPH data was performed and convolved to 0".15 FWHM (not shown). On this image, the jet ends within an angular distance (deconvolved from the 0".15 restoring beam) of about 0".25 ($500h_{100}^{-1}$ pc), or about 0.6 times is deconvolved radius. Higher resolution VLA observations at 2 cm and 3.6 cm are planned to confirm this result.

The southern hot spot is not as rich in total intensity structure as its northern counterpart (Fig. 3*c*). It consists of a bright elongated feature oriented transverse to the jet axis, with filamentary extensions pointing back toward the core. The brightest part of S9 corresponds to a local minimum in the spectral index and the greatest spectral gradient away from the hot spot is in a direction opposite to the core.

Finally, Baby 219 appears to be an independent radio source. It has been optically identified by one of us (A. H. B) with a faint galaxy of unknown redshift. The possibility that Baby 219 is a gravitationally lensed image of 3C 219 can be ruled out because there are no high surface brightness features in Baby 219 like the jet and the hot spots in 3C 219 itself. In addition, it is highly unlikely that the overall shape of a gravitationally lensed image would bear any resemblance to that of the parent source. Gravitational imaging preserves the relative surface brightness of the features while modifying their apparent integrated flux densities, scales, and positions.

Table 4 contains equipartition calculations for some of the features listed in Table 3 as well as typical values for filaments and extended regions of the lobes. The top half of the table uses 22 cm flux densities and low-frequency spectral indices, while the bottom half uses 18 cm flux densities and high-frequency spectral indices. All entries are derived from the data at 1".4 resolution. Note that the minimum pressures in the jet in Table 4 are lower than those estimated previously by BPH, sometimes by an order of magnitude. This is a result of the higher (0".35) resolution of the BPH data, which are more appropriate than the new data for this purpose.

3.2. *Rotation Measure*

The polarization position angle (χ) data from the 20 cm data base were used with the 6, 18, and 22 cm data bases to produce the gray-scale rotation measure (RM) image in Figure 6 (Plate 9). The position angle data were used only where the corresponding polarized brightnesses were greater than 3 times the rms noise levels on the polarization intensity images (Table 2). Where possible, all four position angles were used to determine a best fit value for the RM. In these regions, the formal uncertainty (as determined by the goodness of fit of the χ vs. λ^2 plot) is always less than ± 1.0 rad m^{-2}, and more typically ± 0.1 rad m^{-2}. However, in regions such as the cocoon where the 6 cm polarization data were noisy, the RM was determined from the 18, 20, and 22 cm data alone. In these regions, the uncertainty in the RM is correspondingly higher, typically about ± 4.0 rad m^{-2}.

The RM is generally small, ranging from -25 to $+25$ rad m^{-2}. Local fluctuations between -370 to $+310$ rad m^{-2} are observed, but these values are always confined to very small regions (typically a few pixels), and probably stem from errant data. Note that the choice of the two closest frequencies in the λ^2 domain (1385 and 1465 MHz) allows rotation measures with absolute values less than 320 rad m^{-2} to be determined uniquely.

The structure in the RM is complex and, for the most part, unrelated to the total intensity structures in the source. It is clumpy and in places filamentary. Most of the RM structure is found in the northern lobe and in the region surrounding the jet. In the southern half of the south lobe, the RM is particularly featureless.

The low-resolution studies of Simard-Normandin, Kronberg, & Button (1981) show that the Galactic contribution to the RM of 3C 219 ($l = 174°$, $b = 45°$) is -19 ± 2 rad m^{-2}. Thus, it is possible that much of the observed RM in the southern lobe is Galactic in origin, and not intrinsic to the environment of 3C 219. There may be at least two interesting exceptions where RM detail is associated with 3C 219, however.

The first is in the large-scale emission, or "cocoon," around the jet. The value of the RM changes from -12 ± 4 rad m^{-2} northwest of the jet to $+4 \pm 4$ rad m^{-2} southeast of the jet. In Figure 6, this effect can be seen as two distinctly different levels of gray in the two halves of the cocoon. More sensitive 6 or 3.6 cm polarimetry is needed in order to reduce the uncertainties and to confirm this result. In the jet itself, the average RM is -4.0 ± 0.2 rad m^{-2}. Now, the rotation measure caused by a Faraday screen is given by

$$\mathrm{RM} \propto \int n_e \boldsymbol{B} \cdot d\boldsymbol{l} ,$$

where n_e is the free electron number density, $\boldsymbol{B}$ is the magnetic field vector, and $d\boldsymbol{l}$ is an increment of the distance vector along the line of sight. Thus a sign change in the RM requires a 180° flip in the component of the magnetic field along the line of sight. The simplest configuration for a magnetic field with this property is toroidal (azimuthal). Could the sign change in the RM across the jet in 3C 219 indicate the confining magnetic field outside it, as envisioned in the test proposed by BPH? The integrated flux density over the southeastern half of the cocoon at 22 cm is about 0.2 Jy. Using a spectral index of 1 and approximating the geometry of this region by a cube 15" ($30h_{100}^{-1}$ kpc) on a side, the equipartition magnetic field strength is just under 1 nT (10 μG), yielding an equipartition magnetic energy density of less than 4×10^{-13} J m^{-3}. This is at least an order of magnitude *less* than the equipartition internal energy density estimated for the jet (Table 4). Thus, the magnetic field in the cocoon would confine the jet only if the field were significantly out of equipartition. Note that this conclusion would be reached for any source in which the jet is brighter than the

surrounding cocoon (and therefore distinct from it) because of the intimate connection between the observed surface brightness and the magnetic field strength at minimum energy.

There are two other reasons to believe that this RM pattern is not related to the confinement of the jet. First, the pattern is not smooth. The "excess" of slightly positive RM to the southeast of the jet appears to be part of a filamentary pattern that lies near the jet by chance, rather than a systematic gradient across it. Second, the RM gradient disappears in the region immediately downstream of the visible jet. This should not happen if the gradient is caused by a global structure of the magnetic field in the whole lobe. Figure 7 shows this result quantitatively. Figure 7*a* shows the average values of the RM for regions of width 2″ transverse to the jet and length 15″ parallel to it, as a function of their angular distance from the jet axis. The change in sign of the average RM from one side of the jet to the other is obvious from this plot. In contrast, RM values similarly averaged across the region immediately downstream of the visible jet (Fig. 7*b*) are consistent with a uniform RM in this region.

The second feature in Figure 6 that may be associated with 3C 219 is the compact region of positive RM located just west of the northern hot spot. The fact that this feature is about the same size as the hot spot, and yet not coincident with it, is intriguing. The centroids of the two features are separated by about 12″ (about the diameter of the hot spot itself). There is no associated compact region of negative RM nearby which might indicate a toroidal magnetic field bundle being viewed edge-on.

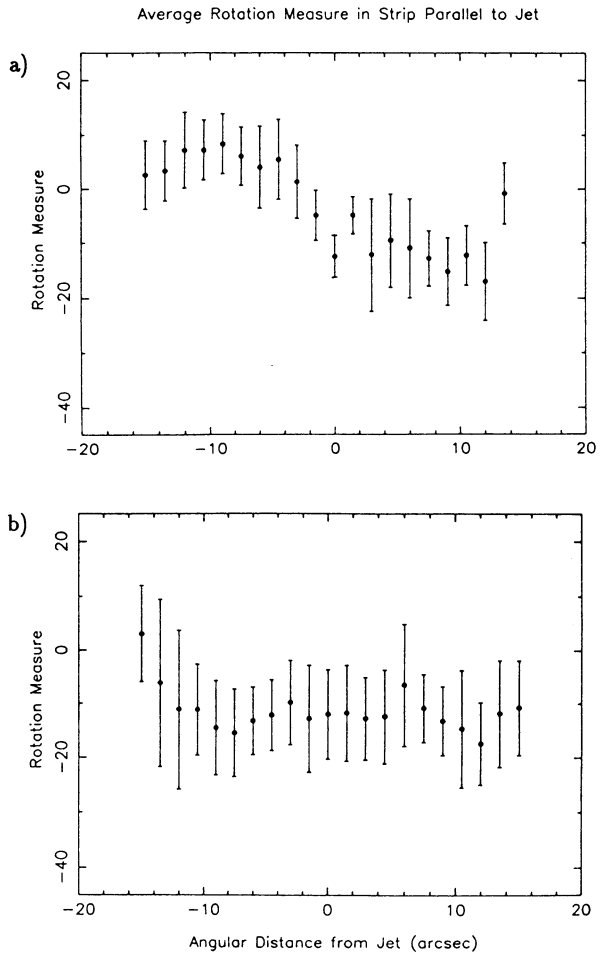

FIG. 7.—Average rotation measure slices across (*a*) the jet and (*b*) the region of the southern lobe just after the apparent end of the jet. Each rotation measure is determined from an average over a 2″ by 15″ strip whose length is parallel to the jet axis.

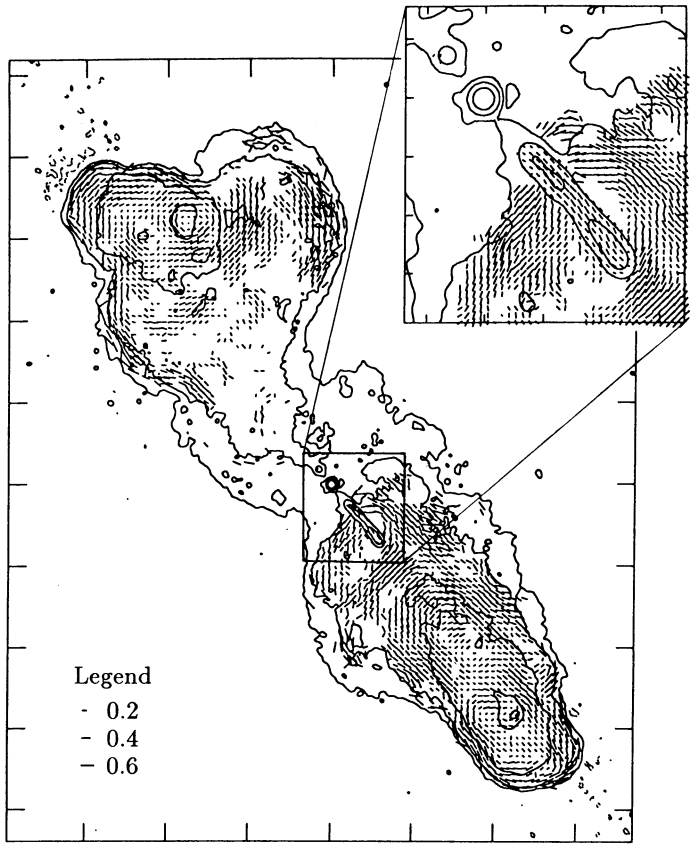

FIG. 8.—Fractional polarization ***B***-vectors (vector lengths are proportional to the 22 cm fractional polarization (see legend) and position angles are those of the inferred magnetic field corrected for Faraday rotation) of 3C 219 superposed on 22 cm total intensity contours (same levels and resolution as Fig. 4). The inset is from the same data and shows more of the polarization ***B***-vectors in the vicinity of the jet. The angular distance between the tick marks around the perimeter of the main image is 20″ and around the inset is 5″.

3.3. *Fractional Polarization and Depolarization*

Figure 8 shows vectors whose lengths are proportional to the fractional polarization at 22 cm ($f_{22} \equiv P_{22}/I_{22}$) and whose position angles are those of the inferred apparent magnetic field $\boldsymbol{B}_a$ (corrected for Faraday rotation), superposed on contours of the total intensity at 22 cm. Figure 9 is a montage of high-resolution (0.″4, $800h_{100}^{-1}$ pc) 6 cm images of the two hot spots and the jet-core region, showing "fractional polarization ***B***-vectors" (lengths proportional to $f_6 \equiv P_6/I_6$ and directions orthogonal to the observed ***E***-vectors) superposed on contours of the total intensity. The images in Figure 9 have not been corrected for Faraday rotation since these corrections are all less than 2° at 6 cm.

Typical of many powerful extragalactic radio sources, the orientation of the projected magnetic field is everywhere circumferential to the edges of the emission region. This is likely the result of the line of sight grazing the edge of the radio plasma and/or shear between the radio plasma and the external medium (Laing 1980). Over much of the source, the circumferential orientation extends deep into the interior of the lobes and is accompanied by a reduction in the fractional polarization. Unlike other well-resolved sources such as Cygnus A

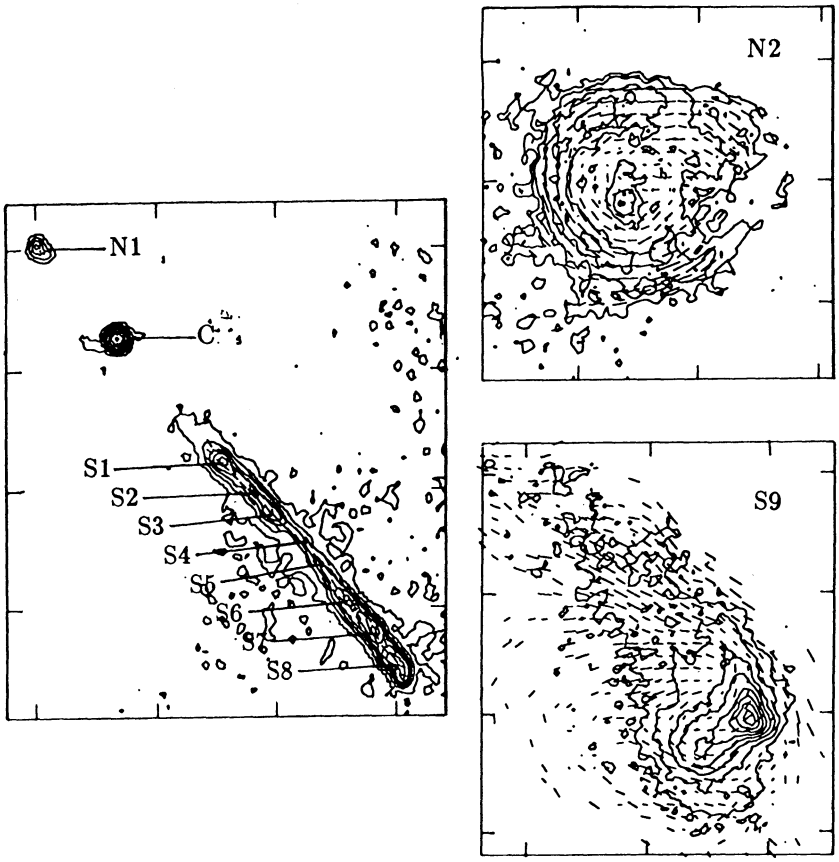

FIG. 9.—Montage of 6 cm, 0.″4 resolution images of fractional polarization ***B***-vectors superposed over total intensity contours of the northern hot spot (*top right*), the jet-core region (*left*), and the southern hot spot (*bottom right*). The angular distance between the tick marks around the perimeter of each image is 5″.

(Dreher et al. 1987, and references therein) and Centaurus A (Clarke 1988) where the projected magnetic field consistently follows the long axis of identifiable total intensity filaments, many of the filaments in 3C 219 do not exhibit this property. This could be a result of confusion by the interfilamentary emission along the line of sight, or it could be an intrinsic property of the filaments in 3C 219. In the case of Cygnus A, Dreher et al. (1987) deduce that the magnetic field and filamentation must be physically related because of the high degree to which the apparent magnetic field follows the features. This conclusion cannot be verified for 3C 219.

Across the northern lobe, the fractional polarization decreases toward the core, falling to less than 10%. The average fractional polarization of the northern hot spot is about 20% at all wavelengths but is edge-enhanced (as high as 35% at 18 and 22 cm, 43% at 6 cm), and decreases toward the interior of the hot spot, reaching a minimum of 10% near the centroid. This should be compared with the total intensity structure, which is also edge-enhanced, decreases toward the interior, but then rises to a peak just south and east of the centroid of the hot spot. There is no corresponding central peak in the fractional polarization. In Figure 9*a*, the polarization ***B***-vectors indicate an apparent azimuthal magnetic field around the center of the hot spot. Figure 8 shows that this pattern extends well away from N2 and dominates the apparent magnetic field structure throughout most of the northern lobe. The fractional polarization of knot N1 is only about 6% at all frequencies, and the apparent magnetic field is transverse to the axis joining N1 to the core.

In the southern lobe, the average fractional polarization is about 10% at the hot spot at all wavelengths and increases in the extended ragions toward the core, rising to more than 60% at 18 cm. Within the southern hot spot, the fractional polarization reaches a maximum of about 23% at all wavelengths and is coincident (within a 1.″4 CLEAN beam) with the local maximum of the total intensity. It then falls off most rapidly in the direction away from the core. Figure 9*c* shows that the apparent magnetic field is parallel to the jet axis on the side of the hot spot nearest the core and pivots about S9 forming an apparent vortex to the east. In addition, there are numerous long, narrow regions of low fractional polarization which lace the southern lobe, some of which demarcate the perimeter of S9. These features could either be geometrical in origin, or could be caused by underresolving the magnetic field structure in the source. In either case, they are probably "sheets" of low fractional polarization in three dimensions rather than "filaments." If, however, they are caused by underresolving boundary layers between neighboring flow structures, they could serve as secondary demarcators of physically distinct features in which the total intensity gradients are not as sharp, e.g., the southern hot spot.

Figure 10 shows total intensity and fractional polarization slices across the two hot spots to illustrate their qualitatively different behavior. The slices across N2 (north-south direction) show a local minimum in the fractional polarization at the centroid of the feature and no local maximum to correspond with the central peak in the total intensity. Both the total intensity and fractional polarization then reach local maxima at the edges of the hot spot. In contrast, the slices across S9 (parallel to the jet axis) show that both the total intensity and fractional polarization are centrally peaked with no edge enhancement. Both quantities fall off most rapidly on the downwind side of the feature. Note that the fractional polarization reaches a local minimum on each side of the southern hot

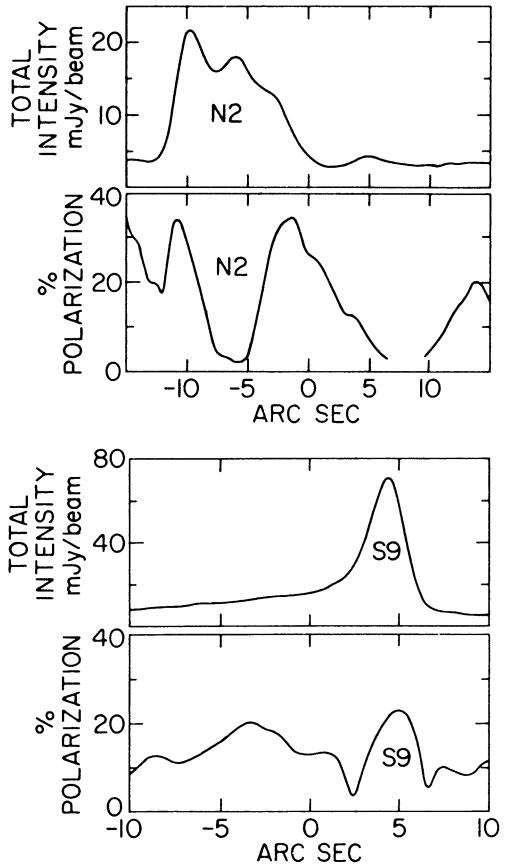

FIG. 10.—Slices of the total intensity and fractional polarization at 22 cm (1.″4, $2.8h_{100}^{-1}$ kpc resolution) across (*top*) the northern hot spot (north-south) and (*bottom*) the southern hot spot (northeast-southwest, parallel to the jet axis). Across the northern hot spot, the fractional polarization is a maximum at the two edges, and a minimum at the center. Conversely, the fractional polarization at the southern hot spot is a minimum at the edges, and a maximum at the center. Note that error bars on the slices are generally too small to plot. For N2, the uncertainties in the fractional polarization range from $\pm 0.2\%$ to $\pm 1.0\%$ while at S9, they range from $\pm 0.1\%$ to $\pm 0.5\%$.

spot, corresponding to the sheet of low fractional polarization demarcating the feature.

At 6 cm, the fractional polarization of the jet ranges from 15% at the apparent beginning and ending of the jet, to about 40% near the center. This is somewhat less than the 60% reported by PBWF at similar angular resolution. The new values should be more reliable as the signal-to-noise ratio is higher for these data than for those of PBWF. At 22 cm, the range is from less than 10% to nearly 35%. In the lobe, the fractional polarization reaches 50% at 6 cm, and between 25% and 30% at 22 cm. In Figure 9*b*, the polarization ***B***-vectors indicate a predominantly axial apparent magnetic field $\boldsymbol{B}_a$ along the axis of the jet, as previously noted by PBWF and BPH. $\boldsymbol{B}_a$ remains axial even at the jet knots, but as soon as the jet disappears, $\boldsymbol{B}_a$ flips by 90° (Fig. 8) and remains transverse to the jet axis for most of the distance between the jet and the hot spot. Of particular note is an elongated region of enhanced fractional polarization which continues from where the total intensity of the jet abruptly ends and extends along the jet axis for about a jet length. The average fractional polarization in this "jet extension" is greater than that in the jet itself, reaching a maximum of $64\% \pm 3\%$ at 18 cm. Two prominent edge-on sheets of low fractional polarization demarcate the edges of the jet and then run parallel to a plausible extrapolation of the edges of the jet towards the southern hot spot. Section 5 offers an explanation for these "sheets."

Figure 11 (Plate 10) is an inverse gray scale image of the depolarization between 6 and 18 cm ($d_6^{18} \equiv f_{18}/f_6$), i.e., the brightest areas correspond to the lowest values of d_6^{18} and are therefore the most depolarized. Data are shown only where the brightness of all four constitutive images exceed 5 times the estimated rms noise. Note that this criterion is more severe than the one used for the fractional polarization and spectral index images. The depolarization structure in Figure 11 shows little correlation with the structure in either the total intensity or the fractional polarization. The depolarization is modest ($d_6^{18} \sim 1$) and featureless (other than statistical fluctuations) over most of the source. In most of the southern lobe, the southwestern half of the jet, and parts of the northeastern half of the northern lobe, the data are consistent with no depolarization ($d_6^{18} = 1$). Moderate depolarization is found in the northeastern half of the jet ($d_6^{18} \sim 0.8$), in the central region of the southern lobe ($d_6^{18} \sim 0.7$) and in the southern ($d_6^{18} \sim 0.7$) and western ($d_6^{18} \sim 0.8$) regions of the northern lobe. At the total intensity peak of the northern hot spot, $d_6^{18} \sim 0.8$, although the average value of d_6^{18} inside N2 is about 1. In the few small regions of the lobe where the depolarization can be estimated, $d_6^{18} \sim 0.6$, although the uncertainties are as much as 40%. Between 18 and 22 cm, there is no compelling evidence of depolarization anywhere in the source.

Severe depolarization ($d_6^{18} \lesssim 0.2$) is localized to several narrow filamentary structures (all less than 12″ long) near the jet and in the southern and western regions of the northern lobe. These appear as bright elongated features in Figure 11. Note that these features are not the result of statistical fluctuations. They represent a second type of filamentation in 3C 219, independent of the total intensity filaments discussed previously. The depolarization filaments are strongly correlated with edges of RM features, i.e., with strong RM gradients (compare Figs. 6 and 11). Both the rotation measure and the depolarization features suggest that a clumpy medium surrounds (or at least lies in front of) 3C 219. There is an excess of such filamentary and clumpy depolarization and RM features in the northern lobe and around the jet. This suggests that the lines of sight to the northern lobe and the jet intersect more of a fragmented and filamentary medium outside 3C 219 than do the lines of sight to the outer part of the southern lobe. This agrees with the effect discussed by Garrington et al. (1988) and Laing (1988) from which the "jetted" lobes of a sample of powerful radio sources were inferred to be closer to the observer than the "jetless" lobes. In the case of 3C 219, there is direct evidence for an asymmetry in the *distribution* of local depolarization features, rather than a smooth global depolarization asymmetry between the two lobes. It will be important to investigate whether the environments of the sources in the samples of Garrington et al. (1988) and Laing (1988) also show such direct evidence of filamentary and clumpy Faraday screens at high resolution.

4. "RESTARTING JET" MODELS FOR 3C 219

Models which address the strong brightness asymmetry of large-scale jets in otherwise symmetric classical doubles can be divided into two main categories according to whether or not the synchrotron emissivity is assumed to trace the energy flux from the radio core to the lobes. The "relativistic beaming" model, in which the brightness asymmetry of the two jets is

attributed to the Doppler selection of two relativistic, kiloparsec-scale jets lying nearly along the line of sight (Scheuer & Readhead 1979; Blandford & Königl 1979), belongs to the category in which the absence of a jet on a synchrotron emission image does not imply that there is no jet. Another model in this category is the "passive field" model of CNB, which is discussed in § 5.

This section discusses the second category of models, in which the lack of a jet segment on a synchrotron emission image may indicate an interruption of the outflow. If the extended lobes of classical doubles are reservoirs of thermalized jet material (Begelman, Blandford, & Rees 1984), then the "jetless" lobe must have had an energetic jet feeding it in the recent past (certainly within the synchrotron half-life of the radio plasma). Thus, a feature common to all models in this category is an "intermittent" or "restarting" jet (Christiansen 1973). Such a jet would require a mechanism at the radio core capable of stopping and restarting the outflow (e.g., the "clamshell" mechanism proposed by Icke 1983) and the time between successive launchings of the jet (the "duty cycle") could vary over the lifetime of the source.

The "restarting jet" model may be particularly applicable to 3C 219 because it naturally produces "partial jets." Presumably, if a jet were intermittently stopped and then restarted, there should be a finite probability of observing a jet in a partial phase. 3C 219 is one of a small subset of 3C radio sources in which a well-defined jet near the radio core "disappears" before reaching its presumed terminus in the lobe. The other known examples are 3C 277.3 (van Breugel et al. 1985), 3C 33.1 (Rudnick 1985), 3C 288 (Bridle et al. 1989), 3C 228 (J. P. Leahy, unpublished), and 3C 445 (W. J. M. van Breugel, in preparation) all of which have approximately the same total radio power as 3C 219.

The first type of "restarting jet" model to be devised was the unipolar "flip-flop," or "alternating ejection" model (Christiansen 1973; Rees 1976; Willis, Wilson, & Strom 1978; Rudnick & Edgar 1984). This model postulates intrinsically unipolar, nonrelativistic outflow to explain the asymmetries of jets in classical doubles without invoking bulk relativistic effects on kiloparsec scales. Applying the "flip-flop" model to 3C 219, the two partial jets could be a result of an unusually short "duty cycle" (compared to the source lifetime) while both lobes are the remnants of jets from earlier epochs. The present main jet, perhaps only a few hundred thousand years old, is boring its way through the old jet material. This model would suggest that activity on this side of the core has recently decreased, giving rise to the "gap" between the core and S1 (notwithstanding the faint emission feature in Fig. 2 connecting the core with S1). Knot N1 indicates the corresponding recent increase in activity on the other side of the core. As discussed by BPH, the ad hoc nature of the "flip-flop" model makes it difficult to establish or refute from the observations. Its only prediction is that the positions (relative to the radio core) of the emission knots in the jet and the lobe on one side of the nucleus should correspond to those of the emission gaps on the other, reflecting the alternating outbursts on either side. Indeed, knot N1 is closer to the core than knot S1, but this is the extent of such correlations in 3C 219. Bulk relativistic motion is compatible with the "flip-flop" model, but the resulting time-of-flight effects drastically complicate the model's prediction of anticorrelated emission knots and gaps for jets near the line of sight. The discovery that depolarization asymmetries correlate almost perfectly with jet sidedness (Garrington et al. 1988; Laing 1988) has given support to the idea that jets in Class II sources (Fanaroff & Riley 1974) lie well out of the plane of the sky and that the observed jet is pointing toward the observer. Thus, it seems plausible that relativistic effects may contribute directly to the asymmetries observed in powerful Fanaroff-Riley Class II sources.

A bipolar "restarting jet" model which incorporates time-of-flight and relativistic effects is the "born-again relativistic jet" model. This was proposed by BPH following their discovery of the counterjet in 3C 219 and may be applicable to other moderately powered sources with "partial jets" (Bridle 1988; Bridle et al. 1989). The model postulates long-term variability of the central engine, mildly relativistic flow velocities, and bipolar outflow without a "flip-flop" mechanism. It predicts, in sources whose main jet disappears before reaching the hot spot in the lobe, that the tip of the (receding) counterjet will appear closer to the nucleus than the tip of the (approaching) main jet (time-of-flight effects of the relativistic flow), that the brightness ratio of the main jet to counterjet will be lower at the tips than nearer the core (shock deceleration of the flow at the tips), and that the synchrotron spectrum of the counterjet will be steeper than that of the main jet (differential Doppler shifting of any spectral curvature). All three of these predictions have been matched to the partial jets in 3C 288 (Bridle et al. 1989), a moderately powerful source that is difficult to classify in the Fanaroff-Riley scheme.

In this model, the abbreviation of the main jet and the counterjet in 3C 219 are real, and the brightness ratios and geometrical asymmetries between them are explained entirely by Doppler favoritism and time-of-flight effects. As pointed out by BPH, the model explains why so little of the counterjet in 3C 219 is seen and why the leading edge of the counterjet (knot N1) is closer to the core than the leading edge of the main jet (knot S8). The fact that N1 is also closer to the core than S1 is coincidental.

The new observations test the remaining prediction of the "born-again relativistic jet" model by providing spectral information for knots N1 and S8. Between 6 and 18 cm, knot N1 has a steeper spectrum ($\alpha_6^{18} = 0.83 \pm 0.03$; see Table 3) than knot S8 ($\alpha_6^{18} = 0.708 \pm 0.005$), in agreement with the model. However, between 18 and 22 cm, the situation is reversed and knot N1 has a flatter spectrum ($\alpha_{18}^{22} = 0.6 \pm 0.1$) than knot S8 ($\alpha_{18}^{22} = 0.76 \pm 0.02$). The spectral curvature required to explain the spectral difference is therefore present in N1 but not in knot S8. Thus, the high-frequency spectra of the two knots encourage the "born-again relativistic jet" model while the low-frequency spectra do not.

Since the bipolar restarting jet model accounts for many of the observed asymmetries between the main jet and the counterjet in both 3C 219 and 3C 288, an axisymmetric numerical simulation of a restarting jet was performed to explore the model's self-consistency. A full account of this calculation is given in Clarke & Burns (1991). Among the results of this simulation, the following are particularly relevant to 3C 219. First, the restarted jet moves through the thermalized material of the original jet (cocoon), which is substantially different from the medium through which the original jet propagated. The hot cocoon gas from the original jet has come into rough pressure balance with the quiescent ambient gas and is therefore less dense than the initial ambient medium. Thus, the density ratio between the restarted jet and its ambient medium is greater than unity (i.e., the restarted jet is *over*dense) giving rise to a somewhat ballistic jet whose working surface

advances with a speed greater than that of the original jet. In addition, the internal shocks in the restarted jet are weaker than those in the original, *under* dense jet. Similarly, the higher temperature in the cocoon gas implies a higher external sound speed. The working surface of the restarted jet therefore advances with a lower Mach number than that of the original jet and the bow shock excited by the passage of the restarting jet is weaker than that excited by the original jet.

Second, the bow shock and the terminal Mach disk in the jet are complementary shocks and should be of comparable strength (as measured by the pressure jumps across them). Thus, on a radio image, they should result in emission features with similar brightness contrasts relative to their immediate surroundings. In short, if a bright partial jet is observed with distinct internal structures, then a feature distinguishable from the background cocoon (the bow shock) should be observed leading the jet. Conversely, if there is no visible bow shock, the partial jet emission should be weak and uniform. Most partial jets in the 3C catalog, including those in 3C 219, are bright and nonuniform, yet there is no feature clearly resembling a bow shock in the extended emission.

Third, the simulation shows little sign of the compact hot spot associated with the working surface of the original jet. Once the jet is terminated, the hot spot is free to expand, and dissipates long before the restarted jet can reach it to resume confinement. This is contrary to the observations of 3C 219. In principle, a shorter, duty cycle could permit the hot spot to survive between successive epochs of jet activity. Also, it is conceivable that microphysical processes not incorporated into the computation play a role in confining the hot spot after the momentum transport by the jet has ceased. These processes include thermal and synchrotron instabilities, in which energy losses from compressed hot spots allow them to cool and thus collapse (Christiansen, Rolison, & Scott 1979), and magnetic confinement.

Comparison of this single simulation of a restarted jet with the data for 3C 219 is therefore inconclusive. The lack of an observed bow shock, and the presence of bright hot spots, in 3C 219 is contrary to the simulation. These discrepancies may, however, be partly explained in terms of the parameters chosen for the simulation and its lack of microphysical processes. Thus, the calculation does not encourage a restarting jet model for 3C 219, but it cannot rule it out either.

5. A PASSIVE MAGNETIC FIELD MODEL FOR 3C 219

The jet simulation of CNB was initialized with the same jet parameters as those in the restarted jet simulation except that the outflow was never interrupted. This simulation was used to compute the synchrotron emission and polarization properties of the jet for a variety of angles between the jet axis and the line of sight (δ) and pitch angles for the magnetic field specified at the jet orifice [$\gamma \equiv \tan^{-1}(B_\phi/B_z)$]. This section compares these numerical models with the radio observations of 3C 219 presented in § 3.

Figure 12 illustrates the anatomy of the CNB jet. The jet enters the computational grid from a small orifice at the left boundary and propagates supersonically toward the right. Ram pressure between the jet and ambient media disturbs the initial pressure (or force) balance, resulting in the pattern of highly oblique criss-cross shocks along the first third or half of the jet. Once force balance has been regained, the jet propagates in a more laminar fashion until the jet material reaches the working surface. Here, the momentum of the jet is thermalized by the Mach disk and shocked jet material is deflected back by the bow shock inflating a hot cocoon surrounding the jet.

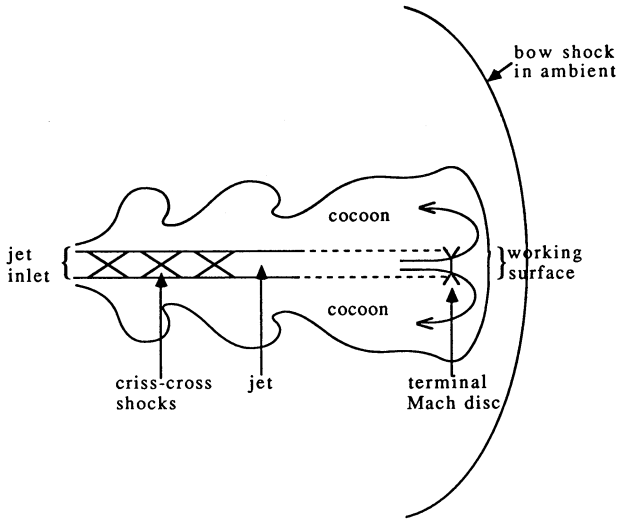

FIG. 12.—Anatomy of the simulated hydrodynamical jet discussed by CNB. The jet enters the computational grid from a small orifice at the left boundary and remains confined to a narrow region about the symmetry axis. During the first third of the jet, it attains force balance with its surroundings, and in so doing, internal oblique "criss-cross" shocks are excited along the axis. Once the shocks terminate, the flow of the jet is more or less laminar until the material reaches the terminal Mach disk. At this point, the kinetic energy is thermalized, and the fluid flows back to inflate the cocoon.

Perhaps the most striking feature of the CNB simulation is that it is sometimes difficult to distinguish the jet emission from that of the cocoon. This is a result of the expansion properties of a toroidal field. Since a flux-frozen toroidal magnetic field (B_ϕ) falls off as r^{-1}, where r is the distance from the symmetry axis, the contribution of the total emission along the line of sight from the cocoon is greater than the emission from the jet itself. Thus, there is no obvious jet "feature," despite the fact that the jet is truly there. On the other hand, a poloidal magnetic field (B_p, confined to a plane perpendicular to the azimuthal direction) falls off as r^{-2} as the jet material expands into the cocoon, and thus the integrated emission along the line of sight from the cocoon is less than that from the jet. In this case, the jet would be easily visible against the background emission. More generally, when both B_ϕ and B_p are present, the jet may be visible over part of its length, but not necessarily over its entire length. The jet will be brightest where the magnetic field is strongest, and this occurs where the axial magnetic field (B_z) is compressed onto the axis by the oblique criss-cross shocks which exist only along the first third of the CNB jet. In principle, these shocks will also compress B_ϕ. However, where the compression by these shocks is the greatest (on the axis), B_ϕ necessarily falls off to zero. Thus, the enhanced emissivity from the first third of the jet is primarily a result of shock compressing B_z rather than B_ϕ. If the jet attains approximate force balance with the immediate surroundings before reaching the terminal Mach disk, the criss-cross shocks will disappear and B_z will no longer be shock compressed. B_z will then expand to fill the volume of the jet, and the emissivity will drop off accordingly. In the study of CNB, the jet emission drops off so suddenly that it essentially disappears into the emission of the cocoon, and only a partial jet is seen in the emissivity image.

Consider the southern lobe of 3C 219 and the CNB jet with

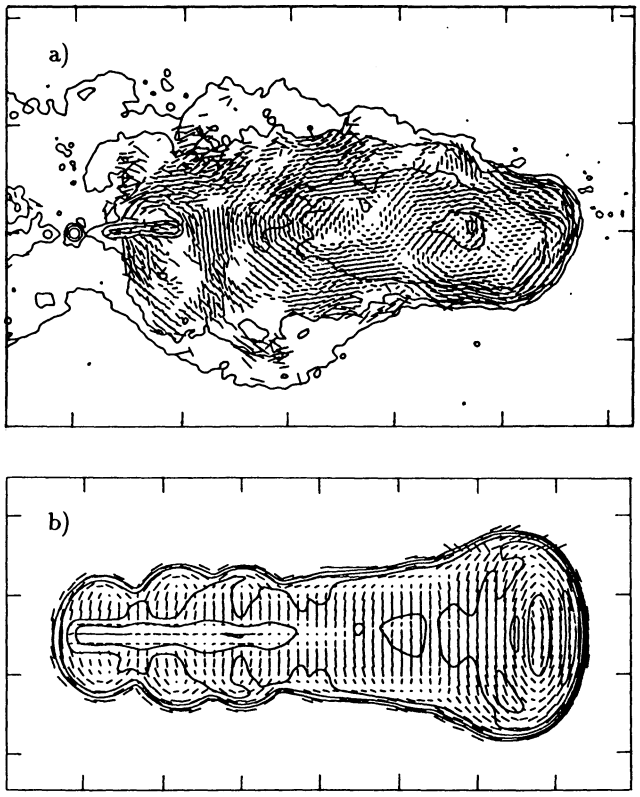

FIG. 13.—Total intensity contours and fractional polarization ***B***-vectors of (*a*) the southern lobe of 3C 219 (Fig. 8) and (*b*) the CNB $\gamma = 30°$, $\delta = 60°$ jet (where γ and δ are defined at the beginning of § 5). The distance between adjacent ticks around the perimeter of (*a*) is 20″ and of (*b*) is five jet radii.

the passive helical magnetic field, shown together in Figures 13 and 14. Figure 14 shows total intensity slices along the axes of the main jet in 3C 219 and the CNB jet. The slices show similar features, including the variation of intensity along the jet itself and the sudden drop of emission over a distance comparable to a jet radius. Second, all along the main jet in 3C 219 and the CNB jet, the $\boldsymbol{B}_a$-vectors are longitudinal to the jet axis and then abruptly flip by 90° just at the point where the jet "disappears" (Fig. 13). Everywhere else, the ***B***-vectors can be divided into two main regions. The first is along the remainder of the jet axis where the vectors are transverse, and the second is the cocoon where they are primarily longitudinal.

The qualitative agreement between the model and the observations is tempered by two possible inconsistencies. First, by choosing different values for γ and δ, the intensity drop in the CNB jet can be made more or less abrupt, but in no case is the drop as sharp as observed in the 3C 219 jet. The CNB jet disappears after the last criss-cross shock is encountered, and thus the jet emission falls off to the cocoon level within a shock cell diameter. In the CNB simulation, this is about two jet radii. If the jet emission in 3C 219 falls off for the same reason, the shock cells in that jet must be about 0.6 of a jet radius (see § 3). It is unclear why the relative sizes of the shock cells in the 3C 219 jet should be a factor of 3 smaller than those in the CNB simulation. Second, unlike the 3C 219 jet, there is no region of enhanced fractional polarization in the CNB jet which extends beyond the bright portion of the jet. This could be a reflection of the epoch and jet parameters chosen for the CNB jet, or it could indicate a problem with the model.

These simulations have several limitations. First, the calculations of CNB are axisymmetric. Since it is not possible to assign a unique value of δ to a real three-dimensional jet, a bend in a jet (caused by free-house instabilities, external magnetic fields, the galactic environment) can alter the polarization characteristics from those typical of one value of δ to another. In addition, the forced axisymmetry of the simulation does not permit the formation of large lobes, which have been produced in slab-symmetric (two-dimensional Cartesian co-ordinates) calculations (Norman et al. 1987; Clarke 1988; Norman & Hardee 1988). The fractional polarization may also be inflated because of the limited degree to which magnetic field lines cross in projection along the line of sight in an axisymmetric calculation.

Second, CNB assume a perfectly conducting, adiabatic fluid. Diffusion of the magnetic field, magnetic reconnection, radiation, thermal and synchrotron instabilities, and relativistic effects are all ignored. The effects of these omissions are not clear, and can be addressed only by more general numerical simulations.

The "passive field" model for 3C 219 is summarized as follows. The southern jet transports a passive helical magnetic field with a small pitch angle, which allows the jet to be traced by its synchrotron emission for a part of its length, but not all of it. In the visible portion of the jet, the axial component of the magnetic field dominates, and gives rise to the longitudinal $\boldsymbol{B}_a$-vectors along its length. The apparent end of the jet marks the location where the jet attains force balance with its immediate surroundings, and the axial component of the magnetic field is no longer shock compressed. Thus, the toroidal component of the magnetic field becomes more important giving rise to the fairly bright lobe and cocoon and to the transverse $\boldsymbol{B}_a$-vectors along the now-invisible jet. It may also be

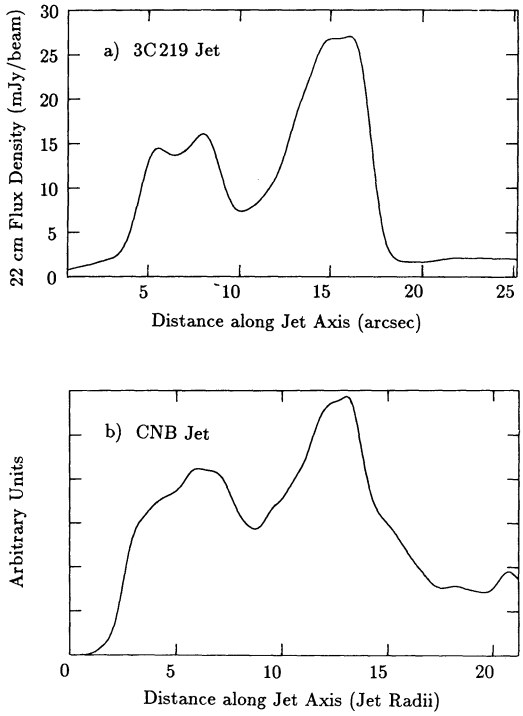

FIG. 14.—Total intensity slices along the axis of (*a*) the 3C 219 jet (Fig. 13*a*) and (*b*) the CNB jet (Fig. 13*b*). For both slices, the core/orifice is to the left, and the apparent terminus is to the right. The gradual increase in brightness along the first 3″ of the 3C 219 jet indicates the faint emission feature joining the core to S1 (§ 4, Fig. 2).

responsible for the modest rotation measure gradient observed in the cocoon, although as discussed earlier, this may be from the Galactic screen or a clumpy medium external to 3C 219. The lobe cannot be too far out of the plane of the sky ($\delta \gtrsim 60°$, say) since an ordered pattern of $\boldsymbol{B}_a$-vectors concentric with the southern hot spot is not distinctive (CNB).

In the northern lobe, the current in the jet is primarily axial and the induced field is therefore toroidal rendering the jet virtually invisible over its entire length. Inside the lobe, the jet is bent in such a fashion that its final trajectory is more or less along the line of sight, giving rise to an elliptical, edge-brightened hot spot, the edge-enhancement of the fractional polarization at N2 (Fig. 10*a*), the elliptical pattern of $\boldsymbol{B}_a$-vectors concentric with N2 throughout the lobe, and the small gradient in the rotation measure.

An advantage of the "passive field" model is its ability to account for the major features in the total intensity and the polarization simultaneously. However, like the restarting-jet models, this model has an ad hoc attribute. No a priori reason can yet be offered for why the main jet should be launched with a primarily axial magnetic field, while the counterjet is launched with a primarily toroidal magnetic field. The model therefore defers, rather than provides, an explanation for the inherent asymmetry of the source. If a mechanism for producing the asymmetry in the magnetic field were discovered, then the "passive field" model could be extended to explain both the one-sidedness and the apparent dominance of longitudinal magnetic fields in the jets of all Fanaroff-Riley Class II radio sources (Bridle 1984, 1988).

Finally, the possibility of active magnetic fields should be mentioned. Clarke, Norman, & Burns (1986); Norman et al. (1987); Clarke (1988); Kössl (1989); and Lind et al. (1989) report some of the first numerical calculations of jets with active magnetic fields. Although the details of the jets are very different when the magnetic field orientation and strength are varied, the common thread that seems to link all jets with a dynamically active magnetic field is they are naked. No cocoon of thermalized back-flowing jet material is formed, even for low-density ratios. Thus, no cocoon exists to obscure the jet even for toroidal magnetic field configurations, and the jet appears as a bright, knotty feature extending all the way from the jet orifice to the tip of the radio plasma. Furthermore, except when viewed nearly along the line of sight, active toroidal magnetic fields do not produce the concentric pattern of polarization $\boldsymbol{B}$-vectors formed when the toroidal magnetic field is passive (CNB). Finally, filamentation in the lobes seems to be characteristic of a passive magnetic field rather than an active one in the limit of ideal MHD (Norman et al. 1987; Clarke 1988). Thus, the circumstantial evidence suggests that the magnetic field in 3C 219 is passive. Sources with active magnetic fields are more likely to be those with naked jets associated with lobes that are confined close to the head of the jet and that show little, if any, filamentation. Powerful radio quasars such as 3C 273 (Conway et al. 1981) and 0800+608 (Shone & Browne 1986) are possible candidates.

6. SUMMARY

High dynamic range VLA images of the radio source 3C 219 have been derived at four frequencies with 1.″4 resolution. The major features of the source include an abbreviated main jet which appears to extend only about one-third of the way from the core to the terminal hot spot; a single elongated knot which may be the brightest part of a counterjet; extended filamentary lobe emission ("cocoon") surrounding the jet and extending away from the major axis of the source; an extended L-shaped hot spot in the southern (main jet) lobe; and an elliptical, edge-brightened hot spot in the northern (counterjet) lobe. Total intensity filaments were observed in most of the extended structure, with a brightness excess of 20% to 25% over the interfilamentary regions of the lobes. A faint emission feature connecting the core and the main jet was detected at 18 and 22 cm. The distributions of spectral index, rotation measure, fractional polarization, apparent magnetic field orientation corrected for Faraday rotation, and depolarization have been derived over the entire source. The spectral index distribution of the extended emission contains evidence for secondary outflow from the hot spots toward the outermost regions of the lobes. The large-scale rotation measure gradients are small and seemingly unrelated to the total intensity features. Confinement of the jet by a strong toroidal magnetic field in the cocoon seems unlikely. Instead, it was concluded that the magnetic field in the jet and lobes is dynamically passive. The apparent magnetic field is longitudinal to the jet axis over the visible portion of the main jet and becomes transverse as the jet "disappears." The apparent magnetic field is everywhere parallel to the boundaries of the lobes, somewhat vorticular in the region near the southern hot spot, and circumferential over a large region surrounding the hot spot in the northern lobe. The depolarization between 18 and 6 cm is slight and clumpy over most of the source. Highly depolarized filamentary features are observed in the northern lobe and around the jet. These features are strongly correlated with large local gradients in the RM. They may indicate a clumpy external medium which obscures the "jetless" northern lobe more than the "jetted" southern lobe of 3C 219, in agreement with the effects reported by Garrington et al. (1988) and Laing (1988).

Two models for the abbreviated appearance of the main jet in 3C 219 have been considered—the "born-again, relativistic" intermittent jet model and a "passive field" uninterrupted jet model. These models differ fundamentally in their assumptions about the relationship between the synchrotron emissivity of the jet and the energy flux transported by the jet.

Both models can explain, or are consistent with, many of the major features in 3C 219. In particular, both are consistent with the brightness asymmetries between the two jets. The "born-again, relativistic jet" model, which *requires* the brightness asymmetries, also accounts for the geometrical asymmetries between the two jets and the high-frequency spectral difference between the tip of the counterjet and the tip of the main jet. Neither of these observations is predicted by the "passive field" model, but both are consistent with it. Both models predict similar ages for the relativistic particles in the hot spots and both hot spots indeed have similar spectral indices and similar energy densities. The "passive-field" model accounts for the polarimetry of both the jet and the lobes in 3C 219 in a self-consistent fashion. However, this cannot be construed as evidence favoring this model over the "born-again, relativistic jet." There is no reason why a restarting jet could not also transport a passive helical magnetic field and thus also create the observed polarization properties in the lobes as in the CNB simulation. The CNB results are quite general, irrespective of jet intermittency, so the polarimetry of 3C 219 is consistent with both models.

Both models have weaknesses. The "born-again, relativistic jet" model is unable to account for the differences in the low-

frequency spectral indices between the tips of the two jets and for the relative compactness of the hot spots. The "passive field" model does not predict the spectral indices but does predict compact hot spots since the energy flow to them is never interrupted. The "born-again relativistic jet" model has a distinct advantage in its ability to account for the very sudden termination of both jets. The "passive field" model may not be able to terminate the main jet as abruptly as observed, and it does not address the appearance of the single bright knot in the counterjet. It is also unable to account for the elongated region of high fractional polarization which extends beyond the point where the jet disappears. The "born-again, relativistic jet" model makes no predictions regarding the polarimetry.

It is difficult to state unequivocally which of the two models for 3C 219 is preferable. The different roles played by the shocks in the two models may, however, provide additional observational discriminants. The "born-again relativistic jet" model invokes strong internal shocks at the advancing tips of the restarting jets (Mach disks) to reduce Doppler favoritism of the main jet over the counterjet (and thus to make the counterjet clearly visible). Mach disks must be accompanied by bow shocks of comparable strength in the surrounding material. In the restarting jet scenario, this material is populated with relativistic electrons and magnetic fields by earlier epochs of jet activity. Thus, a bow shock might be expected to produce an observable feature in the cocoon with a brightness contrast similar to those of features in the jet. In contrast, the "passive field" model does not associate the end of the visible jet with an interruption of the outflow. Thus, no Mach disk and bow-shock are expected at the tip of the jet in this model. In the present data, no bow shock is readily apparent in either lobe of 3C 219, despite the prominence of the jets. Further, since the "born-again relativistic jet" model associates the tip of the jet with a Mach disk, the apparent magnetic field orientation is expected to be transverse at the leading knot. In contrast, the "passive field" model associates the knots in the jet with oblique internal shocks, which will not alter significantly the orientation of a longitudinal or a toroidal magnetic field. Both jets show some evidence of rotation in the apparent magnetic field *at their extreme tips*. However, at the *peak* of the last knot (S8) in the main jet, the apparent magnetic field remains parallel to the jet axis. This is contrary to the restarting jet scenario, and encourages an uninterrupted jet model.

Some of the model predictions could be checked by further high-resolution observations of the internal structure and polarization of the jet, and by additional theoretical investigations. The "passive field" model predicts that the filling factor of the knots in the jets is significantly less than unity. The data of BPH suggest further internal structure, but higher resolution observations are needed to resolve the knots well enough to estimate their filling factors. So far, the evidence for low filling factors in jets is confined to nearby weak sources such as Centaurus A (Clarke, Burns, & Feigelson 1986) and M87 (Owen, Hardee, & Cornwell 1989). The fractional polarization at the knots of the 3C 219 jet tends to be lower than that in the regions between the knots, indicating that the magnetic field structure of the knots may not yet be sufficiently resolved. If higher resolution polarimetry revealed a transverse magnetic field at knots S7 and/or, S8, this would support a restarting jet model. Finally, if a theoretical mechanism to confine hot spots in the absence of jet outflow could be found, then the observation of well defined hot spots in 3C 219 would no longer pose a problem for the "born-again, relativistic" jet model.

We thank J. P. Leahy for producing the MEM images of 3C 219, the NRAO AIPS group for its software, and H. S. Liszt for the *drawspec* software used for the jet profile analysis. We are also grateful to the Department of Astronomy at the University of Illinois for generously making their AIPS processing facilities available to us. This work was partially supported by NSF grants AST-8611511 and AST-9012353 to J. O. B. and M. L. N.

REFERENCES

Baars, J. W. M., Genzel, R., Pauliny-Toth, I. I. K., & Witzel, A. 1977, A&AS, 61, 9
Begelman, M. C., Blandford, R. D., & Rees, M. J. 1984, Rev. Mod. Phys., 56, 255
Blandford, R. D., & Königl, A. 1979, ApJ, 233, 34
Bridle, A. H. 1984, AJ, 89, 979
———. 1988, in Lecture Notes in Physics, 307, Active Galactic Nuclei, ed. H. R. Miller & P. J. Wiita (Berlin: Springer), 329
Bridle, A. H., Fomalont, E. B., Byrd, G. G., & Valtonen, M. J. 1989, AJ, 97, 674
Bridle, A. H., Perley, R. A., & Henriksen, R. N. 1986, AJ, 92 534 (BPH)
Burn, B. J. 1966, MNRAS, 133, 67
Christiansen, W. A. 1973, MNRAS, 164, 211
Christiansen, W. A., Rolison, G., & Scott, J. 1979, ApJ, 234, 456
Clark, B. G. 1980, A&A, 89, 377
Clarke, D. A. 1988, Ph.D. thesis, University of New Mexico
Clarke, D. A., & Burns, J. O. 1991, ApJ, 369, 308
Clarke, D. A., Burns, J. O., & Feigelson, E. D. 1986, ApJ, 300, L41
Clarke, D. A., Norman, M. L., & Burns, J. O. 1986, ApJ, 311, L63
———. 1989, ApJ, 342, 700 (CNB)
Conway, R. G., Davis, R. J., Foley, A. R., & Ray, T. P. 1981, Nature, 294, 540
Cornwell, T. J. 1983, A&A, 121, 281
Cornwell, T. J., & Evans, K. F. 1985, A&A, 143, 77
Dreher, J. W., Carilli, C. W., & Perley, R. A. 1987, ApJ, 316, 611
Dreher, J. W., & Feigelson, E. D. 1984, Nature, 308, 43
Fanaroff, B. L., & Riley, J. M. 1974, MNRAS, 167, 31P
Garrington, S. T., Leahy, J. P., Conway, R. G., & Laing, R. A. 1988, Nature, 331, 147
Hines, D. C., Owen, F. N., & Eilek, J. A. 1989, ApJ, 347, 713
Icke, V. 1983, ApJ, 265, 648
Kössl, D. 1989, in Hot Spots in Extragalactic Radio Sources (Proc. of the Ringberg Castle Workshop), ed. K. Meisenheimer & H.-J. Röser (Berlin: Springer), 225
Laing, R. A. 1980, MNRAS, 193, 439
———. 1985, in Physics of Energy Transport in Extragalactic Radio Sources (Proc. of NRAO Workshop 9), ed. A. H. Bridle & J. A. Eilek (Green Bank: NRAO), 90
———. 1988, Nature, 331, 149
Lind, K. R., Payne, D. G., Meier, D. L., & Blandford, R. D. 1989, ApJ, 344, 89
Macdonald, G. H., Kenderdine, S., & Neville, A. C. 1968, MNRAS, 133, 251
Matthews, T. A., Morgan, W. W., & Schmidt, M. 1964, ApJ, 140, 35
Milne, D. K. 1980, A&A, 81, 293
Norman, M. L., Clarke, D. A., & Burns, J. O. 1987, in Magnetic Fields and Extragalactic Objects (Proc. of the Cargese Workshop), ed. E. Asseo & D. Grésillon (Les Ulis: Edition de Physique), 297
Norman, M. L., & Hardee, P. E. 1988, ApJ, 334, 80
Owen, F. N., Hardee, P. E., & Cornwell, T. J. 1989, ApJ, 340, 698
Perley, R. A., Bridle, A. H., Willis, A. G., & Fomalont, E. B. 1980, AJ, 85, 499 (PBWF)
Perley, R. A., Dreher, J. W., & Cowan, J. J. 1984, ApJ, 285, L35
Rees, M. J. 1976, in The Physics of Nonthermal Radio Sources (Proc. of the NATO Advanced Study Institute), ed. G. Setti (Dordrecht: Reidel), 107
Rudnick, L. 1985, in Physics of Energy Transport in Extragalactic Radio Sources (Proc. of NRAO Workshop 9), ed. A. H. Bridle & J. A. Eilek (Green Bank: NRAO), 35
Rudnick, L., & Edgar, B. K. E. 1984, ApJ, 279, 74
Scheuer, P. A. G., & Readhead, A. C. S. 1979, Nature, 277, 182
Schmidt, M. 1965, ApJ, 141, 1
Schwab, F. R. 1980, Proc. SPIE, 231, 1981
Shone, D., & Browne, I. W. A. 1986, MNRAS, 222, 365
Simard-Normandin, M., Kronberg, P. P., & Button, S. 1981, ApJS, 45, 97
Thompson, A. R., & D'Addario, L. R. 1982, Radio Science, 17, 357
van Breugel, W., Miley, G., Heckman, T., Butcher, H., & Bridle, A. 1985, ApJ, 290, 496
Willis, A. G., Wilson, A. S., & Strom, R. G. 1978, A&A, 66, L1

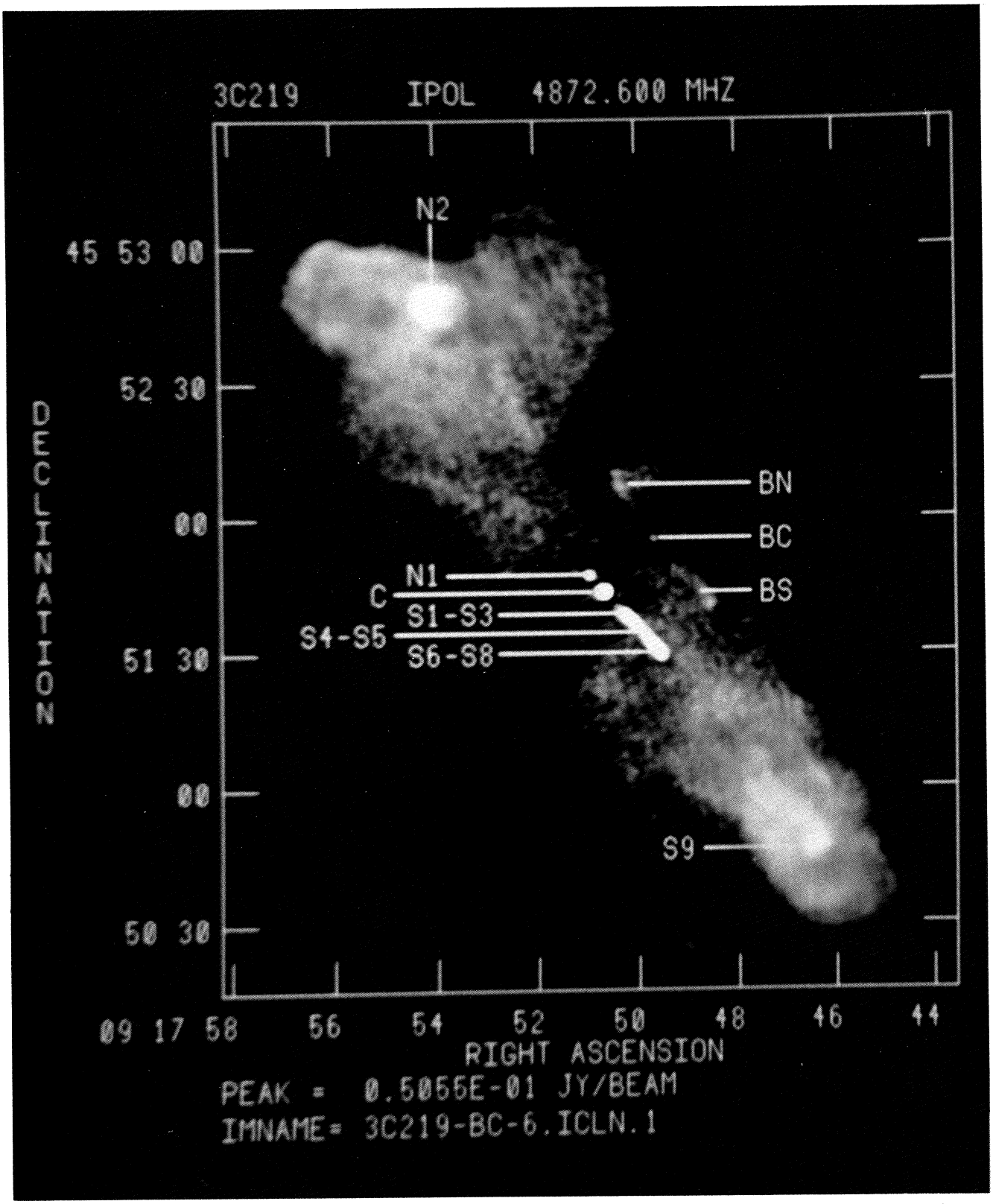

FIG. 1.—Gray-scale, 6 cm total intensity image of 3C 219 at 1.″4 ($2.8h_{100}^{-1}$ kpc) resolution. The various features described in the text are labeled. The gray scale ranges logarithmically from 0 mJy per CLEAN beam (*dark*) to 40 mJy per CLEAN beam (*light*). The peak brightness on the image is 50.6 mJy per CLEAN beam at the core.

CLARKE, BRIDLE, BURNS, PERLEY, & NORMAN (see 385, 175)

PLATE 6

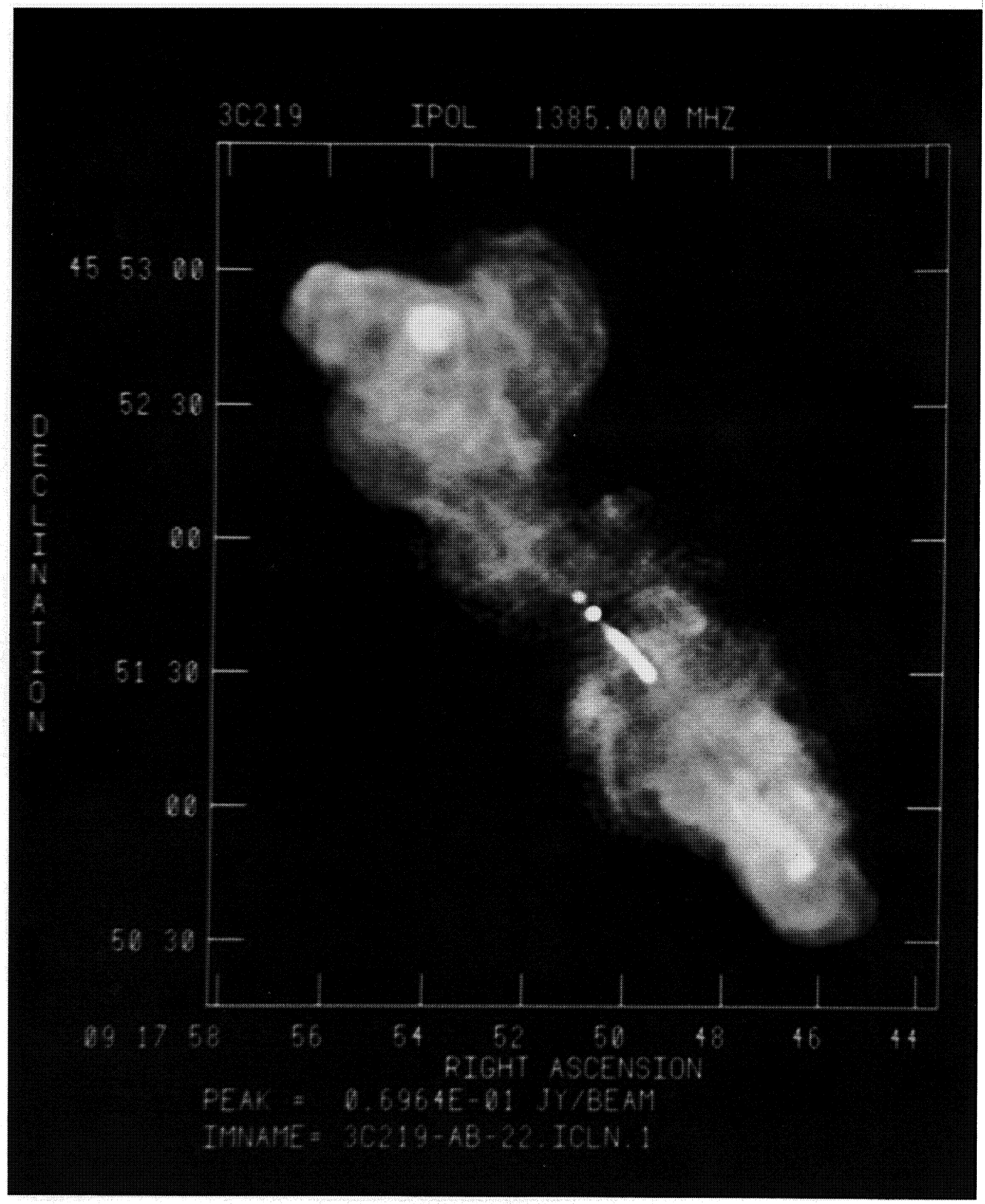

FIG. 2.—Gray-scale, 22 cm total intensity image of 3C 219 at 1.″4 ($2.8h_{100}^{-1}$ kpc) resolution. The gray scale ranges logarithmically from 0 mJy per CLEAN beam (*dark*) to 60 mJy per CLEAN beam (*light*). The peak brightness on the image is 69.6 mJy per CLEAN beam at the southern hot spot.

CLARKE, BRIDLE, BURNS, PERLEY, & NORMAN (see 385, 175)

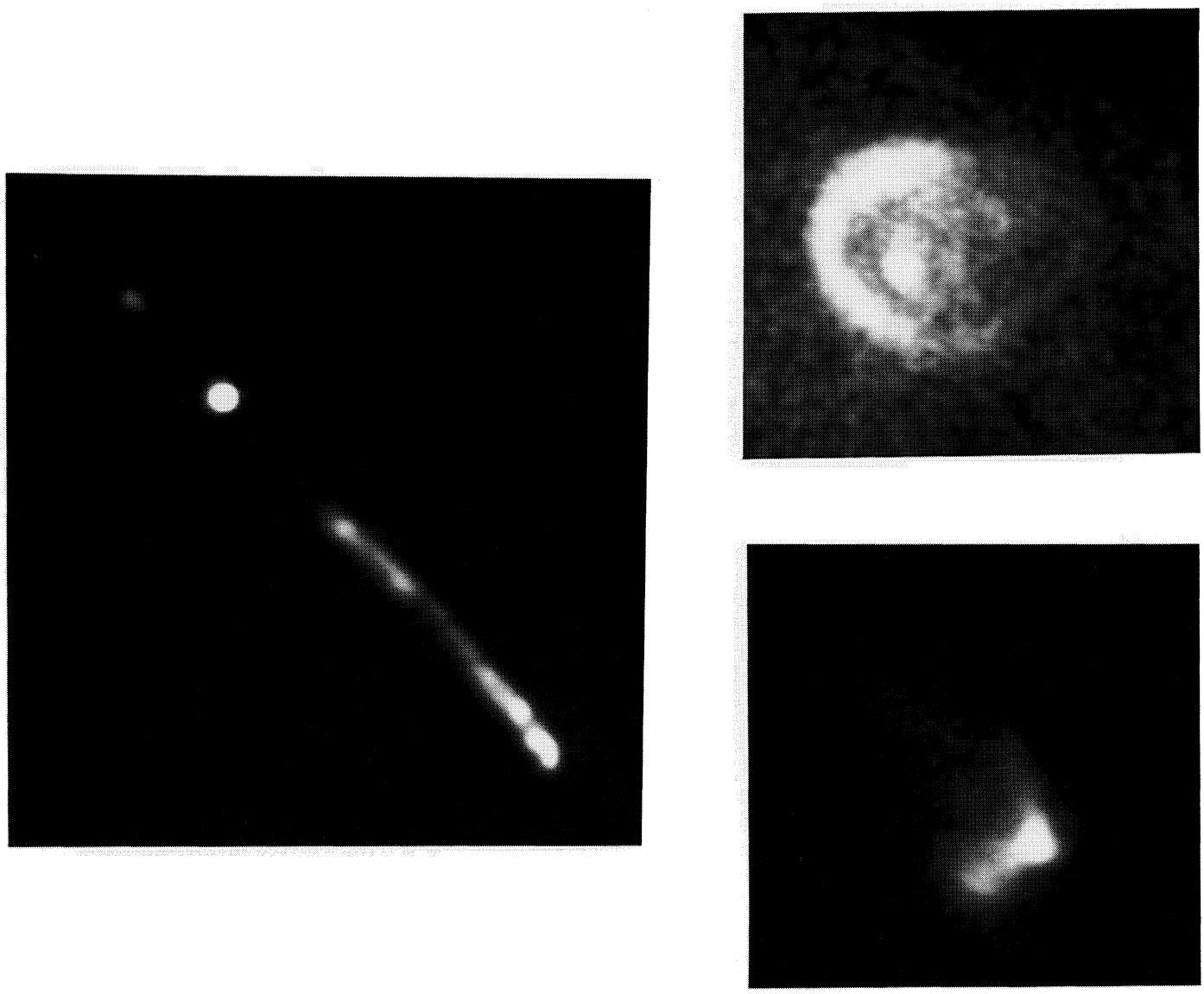

FIG. 3.—Montage of gray-scale, 6 cm total intensity images at 0.″4 ($800h_{100}^{-1}$ pc) resolution of the northern hot spot N2 (*top right*), the jet-core region N1 to S8 (*left*), and the southern hot spot S9 (*bottom right*).

PLATE 8

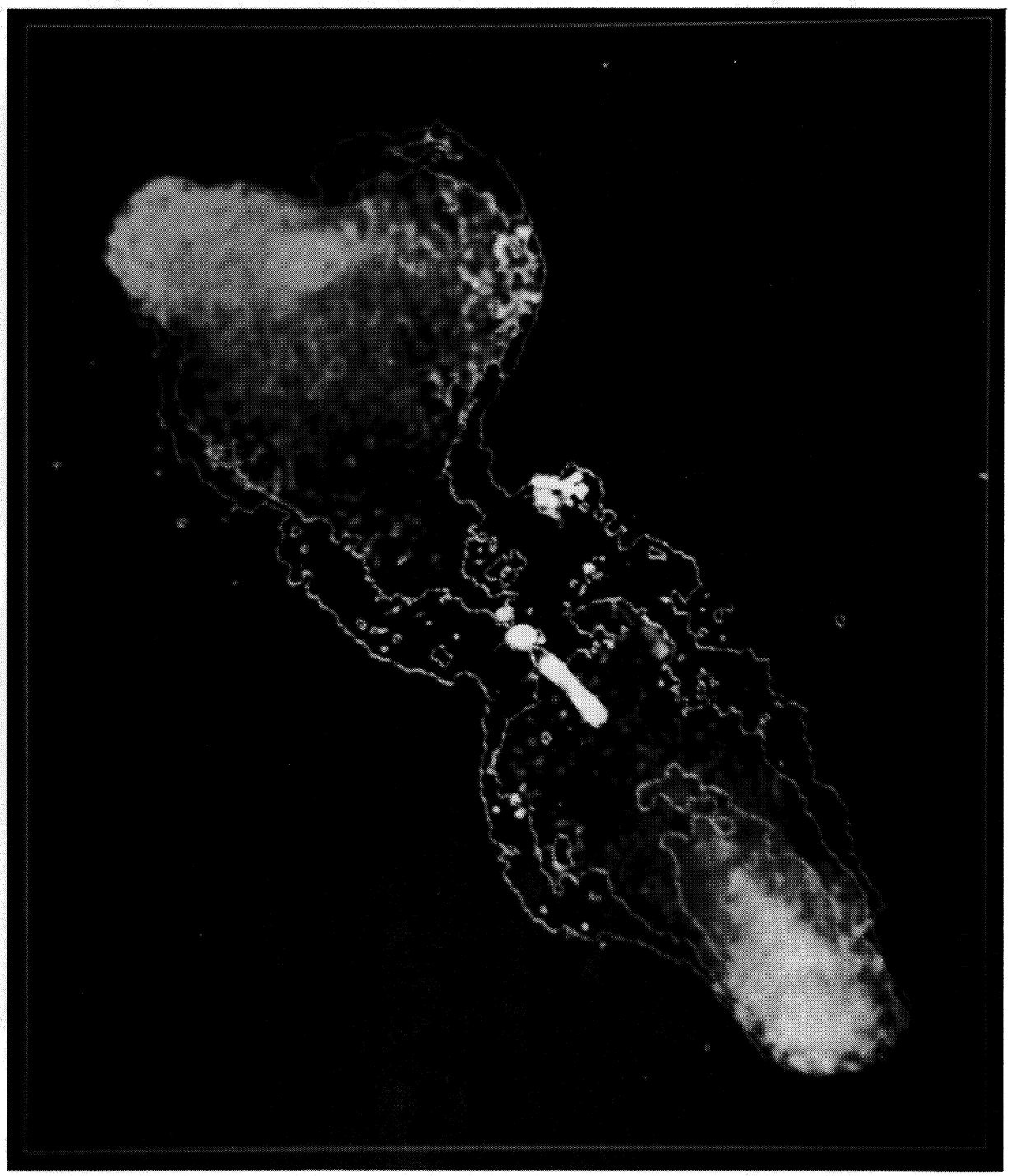

FIG. 4.—Inverse gray-scale, high-frequency (6 and 18 cm) spectral index image of 3C 219 superposed on 22 cm total intensity contours (levels are -1, 1, 4, 16, 64 250×0.2 mJy per CLEAN beam) at 1".4 ($2.8h_{100}^{-1}$ kpc) resolution. The gray scale ranges linearly from 0.7 (*light*) to 2.0 (*dark*) so that regions of low spectral index appear bright. Data are shown only where both brightnesses are greater than 3 times the rms noise. Note that the steepest spectral indices in the most extended regions of the source may be too high by as much as 0.4, since the brightness at 6 cm is somewhat depressed by missing short spacings.

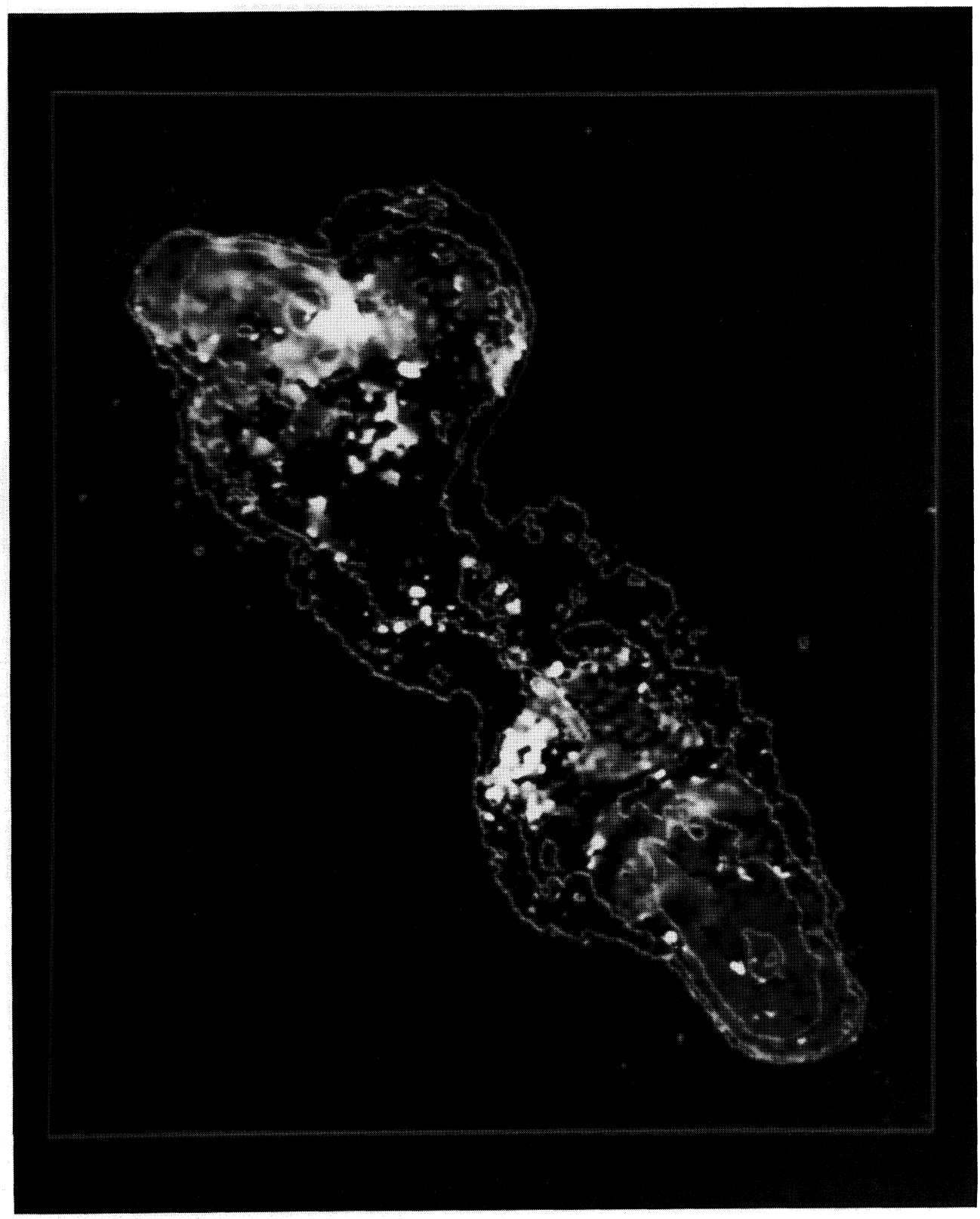

FIG. 6.—Gray-scale rotation measure image of 3C 219 superposed on 22 cm total intensity contours (same levels and resolution as Fig. 4). The gray scale ranges linearly from -25 rad m^{-2} (*dark*) to $+25$ rad m^{-2} (*light*). Data are shown only where the polarized brightness of each contributing image exceeds 3 times the rms noise. The rotation measures for the cocoon and from the western and southern portions of the north lobe were determined from a three-frequency fit. Everywhere else, the values were determined from all four frequencies.

PLATE 10

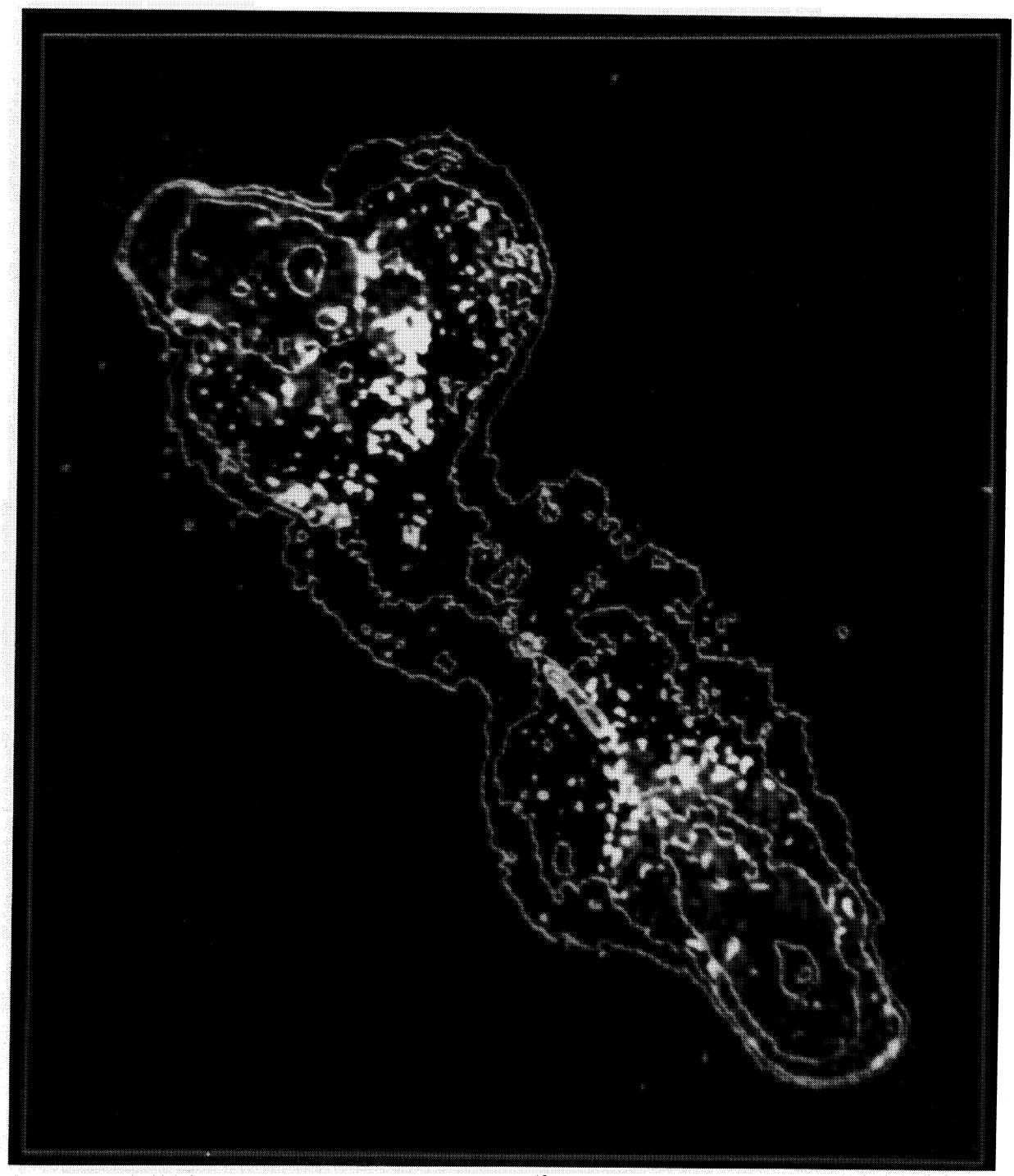

FIG. 11.—Inverse gray-scale, high-frequency (6 and 18 cm) depolarization image ($d_6^{18} \equiv f_{18}/f_6$) superposed on 22 cm total intensity contours (same levels and resolution as Fig. 4). The gray scale ranges linearly from 0.0 (*light*) to 1.0 (*dark*) so that the most depolarized regions appear brightest. Data are shown only where the brightness from each contributing image is greater than 5 times the rms noise.